# Design, Control and Testing of a Pick-and-Place Robot and its Novel Actuators

Thomas Friedlaender

Master of Engineering

Department of Mechanical Engineering

McGill University

Montreal, Quebec

2015-12-12

Thesis submitted to McGill University in partial fulfillment of the requirements of the degree of Master of Engineering (M.Eng.); Mechanical Engineering (Thesis)

## DEDICATION

To those whose care has lead me this far

## ACKNOWLEDGEMENTS

I gratefully acknowledge the tireless support of my supervisor, Jorge Angeles. The invaluable help of professor Takashi Harada, visiting from Kinki University in 2013–2014, is deeply appreciated. The many contributions of the Master's student whose work I continued, Damien Trézières, and of consulting engineer Joe Slanik, are duly acknowledged. I am greatly indebted to my family and friends for their guidance and support. The assistance and advice from students at the Centre for Intelligent Machines and other labs at McGill University is much appreciated.

The support from various sources is to be acknowledged: NSERC (Canada's Natural Sciences and Engineering Research Council), James McGill Professorship to J. Angeles; Japan's MEXT-supported Program for the Strategic Research Foundation to T. Harada; and THK Co. Ltd.

## ABSTRACT

Pick-and-place robots play an important role in industry, performing packaging and assembly tasks. To meet the demand for increasingly fast manipulators, new designs of parallel robots are being developed, as they have distinct speed advantages over their serial counterparts. Recently, a two-limbed, four-degree-of-freedom manipulator with high rotatability of its gripper and an isostatic (fully constrained) structure, the latter improving its assemblability, was introduced. The robot produces Schönflies motion, that is, three independent translations and one rotation about an axis of fixed direction; it is therefore classed as a Schönflies motion generator (SMG). The premiere prototype of this design, termed the PepperMill-Carrier (PMC), was developed and tested, as reported in this thesis. The development of innovative two-degree-of-freedom cylindrical actuators that drive the robot, termed C-drives, is also reported. Workspace analyses and experimental and simulation results are included. The prototypes successfully prove the concepts of the PMC and the C-drive. Recommendations are provided to guide further development.

# ABRÉGÉ

Les robots à transfert rapide jouent un rôle important dans l'industrie et servent à l'emballage et à l'assemblage. Afin de répondre à la demande pour des manipulateurs de plus en plus rapides, de nouveaux concepts de robots parallèles sont actuellement en développement, bénéficiant d'avantages en terme de vitesse par rapport aux robots sériels. Récemment, un manipulateur avec deux jambes, quatre degrés de liberté, une importante mobilité rotationnelle de son effecteur et une structure isostatique a été proposé, cette dernière améliorant l'assemblabilité du robot. Le robot est capable de produire des déplacements du type Schönflies, c'est-à-dire trois translations indépendantes et une rotation autour d'un axe à direction fixe ; il est ainsi désigné générateur de mouvements Schönflies (GMS), ou SMG en anglais. Le premier prototype de ce concept, nommé le « PepperMill-Carrier » (PMC), a été réalisé et testé, tel que décrit dans ce mémoire. La mise au point d'actionneurs cylindriques novateurs à deux degrés de liberté, nommés « C-drives », qui entraînent le robot, est aussi décrite. De plus, des analyses d'espace de travail et des résultats d'expériences et de simulation sont inclus. Les prototypes parviennent à valider les concepts du PMC et du C-drive. Des recommandations sont proposées afin de guider le développement futur du robot.

TABLE OF CONTENTS

DEDICATION . . . . . ii

ACKNOWLEDGEMENTS . . . . . iii

ABSTRACT . . . . . iv

ABRÉGÉ . . . . . v

LIST OF TABLES . . . . . ix

LIST OF FIGURES . . . . . x

1 Introduction . . . . . 1

1.1 Motivation . . . . . 1
1.2 Literature Review . . . . . 4
1.3 Thesis Overview . . . . . 6

2 PMC Displacement and Workspace Analysis . . . . . 7

2.1 Overview of the C-drive and PMC . . . . . 7
2.1.1 Mathematical Modelling of the C-drive . . . . . 7
2.1.2 Design Considerations of the PMC . . . . . 10
2.2 Planar Representation of the PMC . . . . . 11
2.3 Symmetric Architecture of the PMC . . . . . 12
2.4 Displacement Analyses of the PMC . . . . . 13
2.4.1 Inverse Displacement Analysis . . . . . 13
2.4.2 Forward Displacement Analysis . . . . . 16
2.5 Mobility Analysis of the PMC . . . . . 19
2.5.1 Workspace Analysis . . . . . 19
2.5.2 Rotatability Analysis . . . . . 24
2.5.3 Prototype Reachable Workspace . . . . . 25

3 Detailed Design of the PMC . . . . . 27

3.1 Hardware Available at the RMSLab . . . . . 27
3.2 General Dimensions of the PMC . . . . . 27
3.2.1 General Dimensions of the C-drive . . . . . 29
3.2.2 General Dimensions of the PM . . . . . 29
3.3 Detailed Design of the PMC Prototype . . . . . 31
3.3.1 Proximal Link . . . . . 32
3.3.2 Distal Link . . . . . 32
3.3.3 The Hooke Joint . . . . . 33
3.3.4 PM . . . . . 34
3.4 Detailed Design of the C-drive . . . . . 35
3.5 Design of the Collar Middle Part for Testing . . . . . 35

4 Control: Modelling and Implementation . . . . . 39

4.1 Control System Setup . . . . . 39
4.1.1 Overview of Prototype Control . . . . . 39
4.1.2 Computer Hardware Setup . . . . . 39
4.2 C-drive Dynamics . . . . . 40
4.3 Derivation of the State-space Model . . . . . 40
4.4 Controllability and Observability of the C-drive . . . . . 44
4.4.1 Two-dimensional System . . . . . 44
4.4.2 Four-dimensional System . . . . . 44
4.5 Time Response of the C-drive . . . . . 49
4.6 C-drive Controllers . . . . . 51
4.6.1 Ideal PID Controller . . . . . 51
4.6.2 PD Controller Implementation . . . . . 51
4.6.3 Model-based Controller . . . . . 53
4.6.4 Task-space Controller . . . . . 55

5 Experimental Results . . . . . 57

5.1 C-drive Results . . . . . 57
5.1.1 Controller Tuning . . . . . 57
5.1.2 Computed-torque Controller . . . . . 58
5.1.3 TS Controller Tuning . . . . . 59
5.1.4 Benchmark Tests . . . . . 60
5.2 PMC Tests . . . . . 69
5.2.1 Calibration . . . . . 69

5.2.2 Observations . . . . . 70
5.2.3 Industry Standard Test Trajectory . . . . . 71

6 Conclusions and Recommendations . . . . . 72

Appendix A . . . . . 74

Appendix B . . . . . 75

References . . . . . 76

LIST OF TABLES


| Table | | page |
|---|---|---|
| 2–1 | Correspondence between $j$ and inverse/forward conjugate postures | 15 |
| 5–1 | Controller tuning parameters | 59 |
| 5–2 | Scaling coefficients for each motion program | 60 |
| 5–3 | Simulation Parameters | 61 |
| 5–4 | RMS results, 2 Hz tests | 63 |
| 5–5 | Percentage error in RMS simulation predictions, 2 Hz tests | 63 |
| 5–6 | Percentage difference of CT, TS vs. PD controller, 2 Hz tests | 64 |
| 5–7 | Average error at cycle endpoints, 2 Hz tests | 64 |
| 5–8 | Average maximum value over cycle, 2 Hz tests | 64 |
| 5–9 | Experimental 1 Hz results | 65 |
| 5–10 | PMC controller settings | 71 |

LIST OF FIGURES


| Figure | | page |
|---|---|---|
| 1–1 | Examples of serial robots | 2 |
| 1–2 | Examples of parallel PPO robots | 3 |
| 1–3 | Parallel SMG built at McGill University | 4 |
| 2–1 | The C-drive | 8 |
| 2–2 | The standard industry test cycle for SMG | 10 |
| 2–3 | Schematic representations of the PMC | 13 |
| 2–4 | Forward and inverse conjugate postures | 18 |
| 2–5 | Extreme PMC postures | 22 |
| 2–6 | Reachable workspaces | 23 |
| 2–7 | PMC rotatability | 25 |
| 3–1 | Schematic top view of the PMC | 28 |
| 3–2 | Schematic of the C-drive, indicating principal dimensions | 29 |
| 3–3 | Schematic of the PM | 30 |
| 3–4 | 3D CAD rendering of the PMC in its isotropic posture | 31 |
| 3–5 | Whole upper limb | 32 |
| 3–6 | Complete collar | 33 |
| 3–7 | Side view of joint between proximal and distal links | 34 |
| 3–8 | Descriptive view the Hooke joint | 35 |
| 3–9 | Cross section view of the PM | 36 |

3–10 Annotated picture of the C-drive . . . . . 37
3–11 Ballscrew coupling: bearing, housing and shaft . . . . . 37
3–12 Collar components . . . . . 38
4–1 Block-diagram of PID controller, with PI torque control loop . . . . . 52
4–2 Block diagram of computed-torque controller . . . . . 53
5–1 Motion programs and test results for 2 Hz cycles . . . . . 66
5–2 Experimental and simulated test results, 2 Hz cycles . . . . . 67

# CHAPTER 1
# Introduction

## 1.1 Motivation

Many industrial tasks, from food packaging to automotive-parts assembly to electronic-circuit manufacturing, involve manipulating and accurately positioning objects. As these operations are repetitive and well-structured, they lend themselves to automation. The first industrial robot to be developed was the UNIMATE, operated by General Motors starting in 1961 [1]. It was a *serial* robot, i.e., composed of a single open kinematic chain, and produced motion with five (and later six) degrees of freedom (dof). Early robots such as UNIMATE and later the Stanford Arm featured prismatic (sliding) joints in addition to revolute (pin) joints, as this simplified their kinematics [2], an important attribute at a time when microprocessors were in their infancy. The need for higher dexterity and speeds led to the development of serial robots with six revolute joints, notably the 1973 KUKA Famulus, the first industrial robot with six electromechanically driven axes, shown in Fig. 1–1a. Many common pick-and-place operations (PPO) do not require full six-dof manipulation, and are therefore more suited for specialized robots with reduced mobility. An important category of PPO robots are the Schönflies Motion Generators (SMG), capable of generating four-dof motions of their end effector (EE), namely three independent translations and one rotation about an axis of fixed direction, usually vertical. This motion is well illustrated by the movement of a waiter's tray, which is kept horizontal

(a) (b)

Figure 1–1: Examples of serial robots: (a) Several postures of the KUKA Famulus; and (b) the Adept Cobra s350 SCARA robot

at all times. SMG take their name from the Schönflies subgroup $\mathcal{X}$ of rigid body displacements, from the theory of Lie groups [3]. SMG are suited for factory applications on flat surfaces, such as conveyor-belt lines. The first SMG were serial robots termed SCARA (Selective Compliance Assembly Robot Arm), developed by Hiroshi Makino in 1978 [4]. A common robot of this type is shown in Fig. 1–1b. Serial robots are limited in their speed by the need for each motor from the base onward to drive all upstream motors and links. This motivated the development of *parallel* robots—composed of at least two closed kinematic chains—capable of higher speeds at the cost of higher complexity[1]. An excellent analysis of the trade-offs involved is found in [5]. The first parallel robot was the Stewart Gough platform, invented independently at least three times in the 1950s and 60s [6, 7]. The first successful

[1] The economics of choosing parallel vs. serial PPO robots is discussed at http://coro.etsmtl.ca/blog/?p=55.


(a) (b)

Figure 1–2: Examples of parallel PPO robots: (a) The ABB IRB 360 FlexPicker, an augmented Delta; and (b) the Adept Quattro s650H, an instance of H4

parallel four-dof PPO robot is a version of Clavel's Delta, patented in 1990 [8]. The Delta, a generator of the 3D translational subgroup of rigid body displacements, is augmented with one rotational dof, resulting in a SMG, as shown in Fig. 1–2a. The STAR concept, employing parallelogram ($\Pi$) joints like the Delta but driven by helical actuators, was proposed by Hervé and Sparacino [9]. The current fastest parallel SMG is the Adept Quattro, shown in Fig. 1–2b, based on the H4 concept proposed by Pierrot et al. [10]. The rotation of the moving platform (MP) is achieved by a complex amplification mechanism and limited to a half turn. Other problems with the foregoing robots include their complex workspaces, the risk of limb collisions, and difficult assembly, as they are overconstrained, thus requiring extra joints that introduce idle dof, play and compliance. This drawback is absent in *isostatic* (fully constrained) robots, which are, therefore, of interest.

## 1.2 Literature Review

Many efforts have been dedicated to improving the design of parallel SMG. The I4 family of robots was introduced by Krut et al. [11] to address the drawbacks of the H4, such as link collisions when rotating the MP. Richard et al. [12] proposed the partially decoupled four-limb Quadrupteron. Other robot designers have focused on reducing the complexity of parallel robots by proposing two-limb designs [2]. For instance, Angeles et al. introduced the McGill SMG [13, 14], shown in Fig. 1–3a.

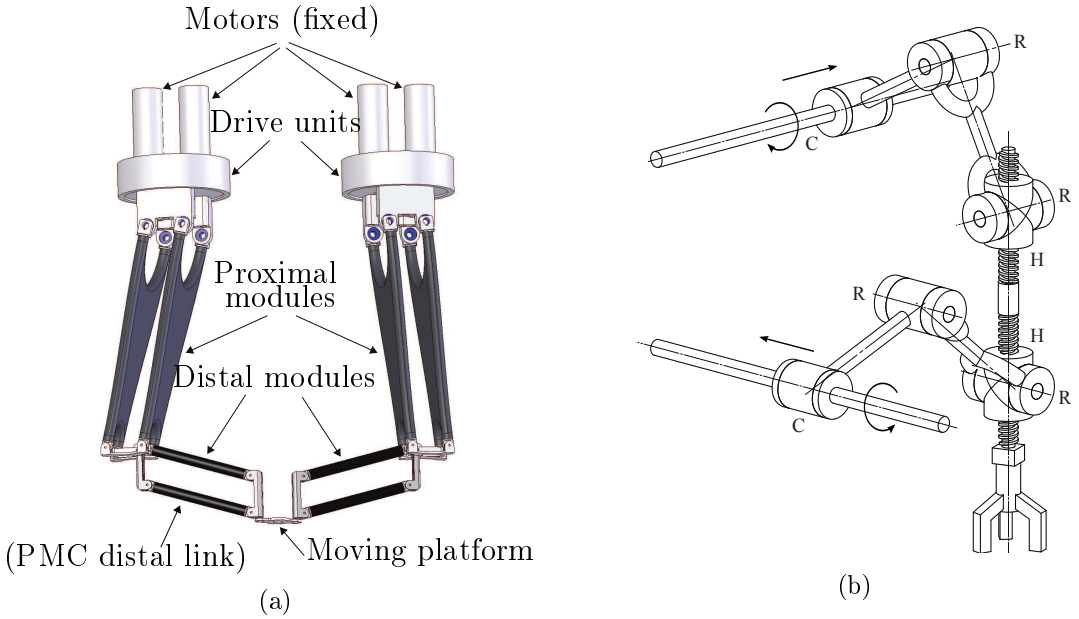


Figure 1–3: Parallel SMG built at McGill University: (a) The first McGill SMG prototype [13]; and (b) one of Lee's ISMG, termed the PepperMill Carrier (PMC)

In their quest to find two-limbed isostatic SMG (ISMG), Lee and Hervé performed a search of all mechanisms resulting from the concatenation of two serial chains producing Schönflies ($\mathcal{X}$)-motion, termed $\mathcal{X}$–$\mathcal{X}$ motion generators [15], later focusing their research on SMG [16]. Based on this work, P.-C. Lee et al. proposed

four new isoconstrained SMG, derived their kinematics and performed workspace and singularity analyses [17, 18, 19, 20]. Harada and Angeles [21] selected one of the designs, shown in Fig. 1–3b, and derived its kinematics and singularity analyses in the presence of two two-dof actuators, termed the C-drives[2]. This ISMG is a symmetric, single-loop kinematic chain of the CRRHHRRC type, where R, C and H denote revolute, cylindrical[3] and helical (screw) joints, respectively. The common link to both limbs is composed of two rigidly connected coaxial screws of different pitches, and termed the *PepperMill* (PM) by analogy with the motion of a large pepper mill. The robot is therefore known as the *PepperMill-Carrier* (PMC). The application of the Chebyshev-Grübler-Kutzbach formula confirms that the PMC has four dof [22], while a Lie group mobility analysis reveals that the four dof are those of the $\mathcal{X}$-subgroup of rigid-body displacements. In addition to being isostatic, the simple differential rotation mechanism of the PMC endows the PM with high rotatability, as the screw pitches and lengths can be varied to obtain a wide mobility range. Furthermore, the limbs cannot collide while the screw nuts are within their stroke length. The principal hurdle in designing a PMC prototype is the embodiment of the cylindrical joints.

[2] One singular posture was found that escaped P.-C. Lee et al. [17].

[3] A cylindrical joint is capable of independent rotations about an axis and translations in the direction of the axis.

## 1.3 Thesis Overview

This thesis reports on the work leading to the development and testing of the novel PMC and its C-drives. Through analyses and experiments, the C-drive and PMC concepts are validated and their performance is ascertained. Chapter 2 builds upon previous research on PMC kinematics to provide means to be used by the PMC control system, as well as workspace analyses to determine the safe operating workspace. Chapter 3 summarizes the mechanical design of the prototype and the principal decisions involved. Chapter 4 reports on the derivations of the C-drive dynamics in state-space form and introduces several control systems for the C-drive. Chapter 5 discusses the experimental and simulation results from prototype testing. Finally, Chapter 6 concludes the work and makes recommendations for further study.

# CHAPTER 2
# PMC Displacement and Workspace Analysis

## 2.1 Overview of the C-drive and PMC

### 2.1.1 Mathematical Modelling of the C-drive

The PMC must be driven by fully actuated cylindrical joints in order to keep the motors fixed to the base. However, no cylindrical drives of this type are commercially available. One six-dof parallel robot requiring such a drive was proposed by Behi [23]. The design of a rotary-linear actuator was subsequently reported by Kohli et al. [24, 25], consisting of a prismatic actuator in parallel with a rotating prismatic joint. The motors are fixed, but loaded and dimensioned differently. A new concept for a cylindrical (C) drive that comprises two identical fixed motors equally sharing the load was recently proposed by Harada et al. [26]. The design process entailed a search for symmetric single-loop kinematic chains of low *complexity*, as defined by Khan and Angeles [27]. The resulting coaxial RHHR chain with actuated revolute joints is shown in Fig. 2–1. Conceptual work on the C-drive and PMC is summarized in an internal report [28]. Preliminary tests were carried out on the C-drive prototype [26], while the results of more advanced experiments and simulations were reported recently [29].

The C-drive comprises two coaxial screws of different pitches. For symmetry, the pitches are given the same absolute value $p_c$, but are of opposite hands. The *collar* is the link coupled to each motor shaft via the screws.

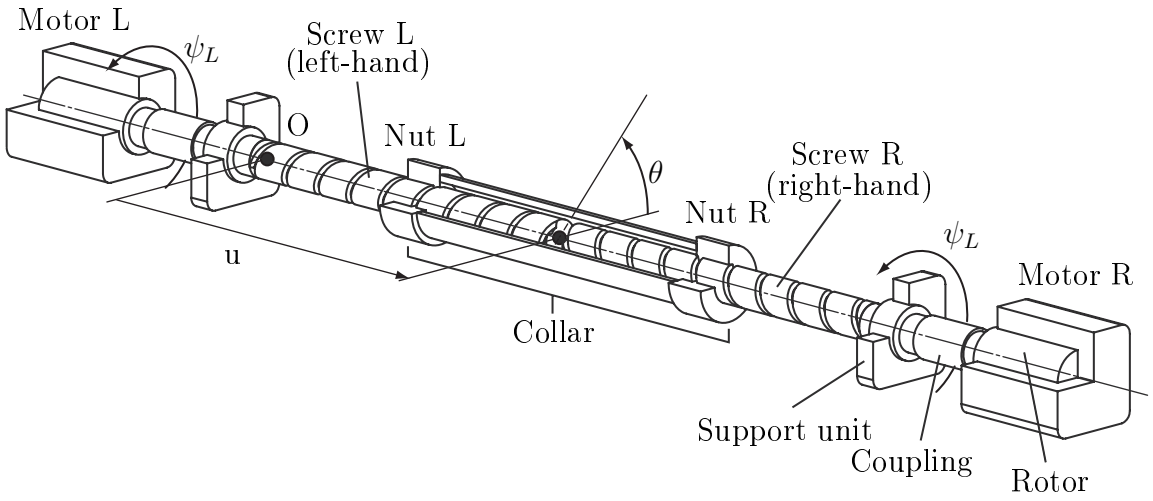


Figure 2–1: The C-drive

**C-drive Kinematics**

The kinematics of the C-drive, as reported earlier [26], is summarized below:

$$\boldsymbol{\psi} \equiv \begin{bmatrix} \psi_L \\ \psi_R \end{bmatrix}, \quad \mathbf{w} = \mathbf{J}\boldsymbol{\psi}, \quad \dot{\mathbf{w}} = \mathbf{J}\dot{\boldsymbol{\psi}} \tag{2.1a}$$

$$\mathbf{w} \equiv \begin{bmatrix} u \\ v \end{bmatrix}, \quad \mathbf{J} \equiv \frac{p_c}{4\pi} \begin{bmatrix} 1 & -1 \\ 1 & 1 \end{bmatrix} \tag{2.1b}$$

where $\boldsymbol{\psi}$ is the vector of joint displacements, $\psi_L$ and $\psi_R$ being the left and right angular motor displacements, respectively, $u$ the translational displacement of the collar, and $v$ a linear transformation of the rotational displacement of the collar, denoted $\theta$, namely,

$$v \equiv \frac{p_c}{2\pi}\theta \tag{2.2}$$

The Jacobian matrix $\mathbf{J}$ is isotropic—its singular values are identical [30]—as $\mathbf{J}^T\mathbf{J}$ is proportional to the $2 \times 2$ identity matrix $\mathbf{1}$:

$$\mathbf{J}^T\mathbf{J} = \frac{p^2}{8\pi^2}\mathbf{1} \tag{2.3}$$

Furthermore the inverse kinematics is given by

$$\boldsymbol{\psi} = \mathbf{J}^{-1}\mathbf{w}, \quad \dot{\boldsymbol{\psi}} = \mathbf{J}^{-1}\dot{\mathbf{w}}, \quad \mathbf{J}^{-1} \equiv \frac{2\pi}{p_c}\begin{bmatrix} 1 & 1 \\ -1 & 1 \end{bmatrix} \tag{2.4}$$

### C-drive Dynamics in Terms of Generalized Coordinates

The dynamics of the C-drive is represented by the mathematical model reported by Harada et al. [26]:

$$\mathbf{M}\ddot{\boldsymbol{\psi}} + \mathbf{D}\dot{\boldsymbol{\psi}} + \boldsymbol{\phi}_c = \boldsymbol{\tau} \tag{2.5}$$

where the generalized inertia matrix $\mathbf{M}$, damping matrix $\mathbf{D}$, vector of Coulomb-friction torques $\boldsymbol{\phi}_c$ and vector of motor torques $\boldsymbol{\tau}$ are defined as

$$\mathbf{M} \equiv \begin{bmatrix} m_{11} & m_{12} \\ m_{12} & m_{11} \end{bmatrix}, \quad m_{11} \equiv I_h + \frac{I_c}{4} + \frac{p_c^2 m}{16\pi^2}, \quad m_{12} \equiv \frac{I_c}{4} - \frac{p_c^2 m}{16\pi^2} \tag{2.6a}$$

$$\mathbf{D} \equiv \begin{bmatrix} d_{11} & d_{12} \\ d_{12} & d_{11} \end{bmatrix}, \quad d_{11} \equiv \beta + \frac{1}{2}\gamma, \quad d_{12} \equiv -\frac{1}{2}\gamma \tag{2.6b}$$

$$\boldsymbol{\phi}_c \equiv \begin{bmatrix} \delta\mathrm{sgn}(\dot{\psi_L}) + \eta\mathrm{sgn}(\dot{\psi_L} - \dot{\psi_R}) \\ \delta\mathrm{sgn}(\dot{\psi_R}) + \eta\mathrm{sgn}(\dot{\psi_R} - \dot{\psi_L}) \end{bmatrix}, \quad \boldsymbol{\tau} \equiv \begin{bmatrix} \tau_L \\ \tau_R \end{bmatrix} \tag{2.6c}$$

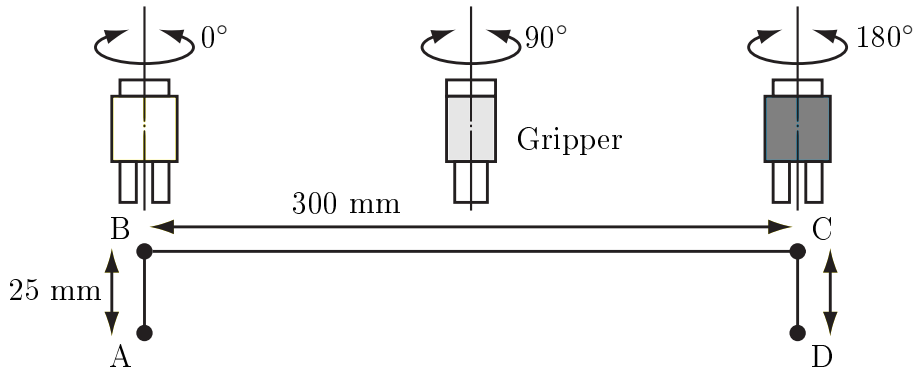


Figure 2–2: The standard industry test cycle for SMG

while $m$ and $I_c$ are the collar mass and moment of inertia about the C-drive axis, $I_h$ is the moment of inertia of the other rotational parts about the same axis, $\beta$ and $\gamma$ are the viscous friction coefficients, while $\delta$ and $\eta$ are the Coulomb-friction coefficients, $p_c$ is the screw pitch, and $\mathrm{sgn}(\cdot)$ is the signum function.

### 2.1.2 Design Considerations of the PMC

#### Standard Industry Test Cycle

In order to compare the performance of different PPO robots, industry has adopted a benchmark test trajectory, as shown in Fig. 2–2. The cycle consists of a 25 mm upward vertical translation, a 300 mm horizontal translation and simultaneous half turn rotation, a 25 mm downward translation, and the same motion in reverse. The PMC is dimensioned to be able to perform this motion. In practice, smoother curves are employed to avoid the discontinuities at points B and C, for example the "Adept Motion" used to test the H4 robot [31]. Gauthier et al. proposed a smoother trajectory based on Lamé curves, to be customized for each robot to reduce the maximum acceleration values of the gripper [32].

**PMC Posture**

The PMC limbs are each composed of the following links: the base, the proximal link, the distal link, the Hooke joint, the PepperMill. The base and PM are shared by both limbs. Each limb has two possible postures, as the "elbow" between the proximal and distal links can be pointed either up or down, resulting in four total postures of the PMC for the same PM pose. The posture with both elbows up is selected for the prototype: the lower elbow is up in order to allow the gripper to be attached directly below the PM, and the upper elbow has the same posture to prevent limb collisions. This posture appears in Fig. 1–3b.

**PMC Dimensions**

The dimensions of the PMC, also referred to as the *architecture* or *layout*, are selected so as to permit the prototype to perform the standard industry test trajectory. The distal links of the PMC were taken directly from the old prototype of the McGill SMG, as indicated in Fig. 1–3a. For reasons of symmetry, the two screws of the PM are assigned pitches of the same absolute value, denoted $p$, the top and bottom screws being left- and right-handed, respectively.

## 2.2 Planar Representation of the PMC

The PMC is represented as an annotated 3D CAD model in Fig. 2–3a, where the point $C$ of the PM has coordinates $(x, y, z)$. A planar representation is now introduced in Fig. 2–3b, which can fully describe any posture of the robot. The respective planes in which the limbs operate are portrayed as being parallel. The translational displacement $d_1$ of the proximal link of limb 1 is equal to the $x$-coordinate of point $P_2$

of the PM, as described in Section 2.4. The equivalent relation holds for the translational displacement $d_2$ of the second proximal link and the $y$-coordinate of point $P_1$ of the PM. Point $C$, the centre of the PM, is defined as the midpoint between points $P_1$ and $P_2$. The $z$-coordinate of the PM is indicated by the distance between $C$ and a line passing through the origin $O$. The orientation $\phi$ of the PM is proportional to the vertical distance $p\phi$ between $P_2$ and $C$. That is, the $x$-, $y$- and $z$-coordinates as well as the orientation $\phi$ of the PM are readily observed in the diagram.

The planar representation of the PMC was found to be extremely useful in visualizing the postures and motions of the robot. It is readily drawn in any commercial CAD package to study postures and design changes, without the need of manipulating complex 3D models. Results in the balance of Chapter 2 were verified using planar diagrams drawn in Solidworks.

## 2.3 Symmetric Architecture of the PMC

Symmetric relations are imposed on the link dimensions of the PMC in order to obtain a modular, simple design. The two limbs are identical, as are the lengths of the proximal and distal links. Furthermore, it is recalled that the PM screw pitches are identical, but of opposite hands. Hence, the symmetric relations are

$$p \equiv p_1 = -p_2, \quad r \equiv r_i = l_i, \quad i = 1, 2 \tag{2.7}$$

where $r_i$ and $l_i$ are the lengths of the proximal and distal links, respectively, while $p_1$ and $p_2$ are the pitches of the screws belonging to the first and second limbs. Only the variables $r$ and $p$ need appear in the analyses of the PMC.

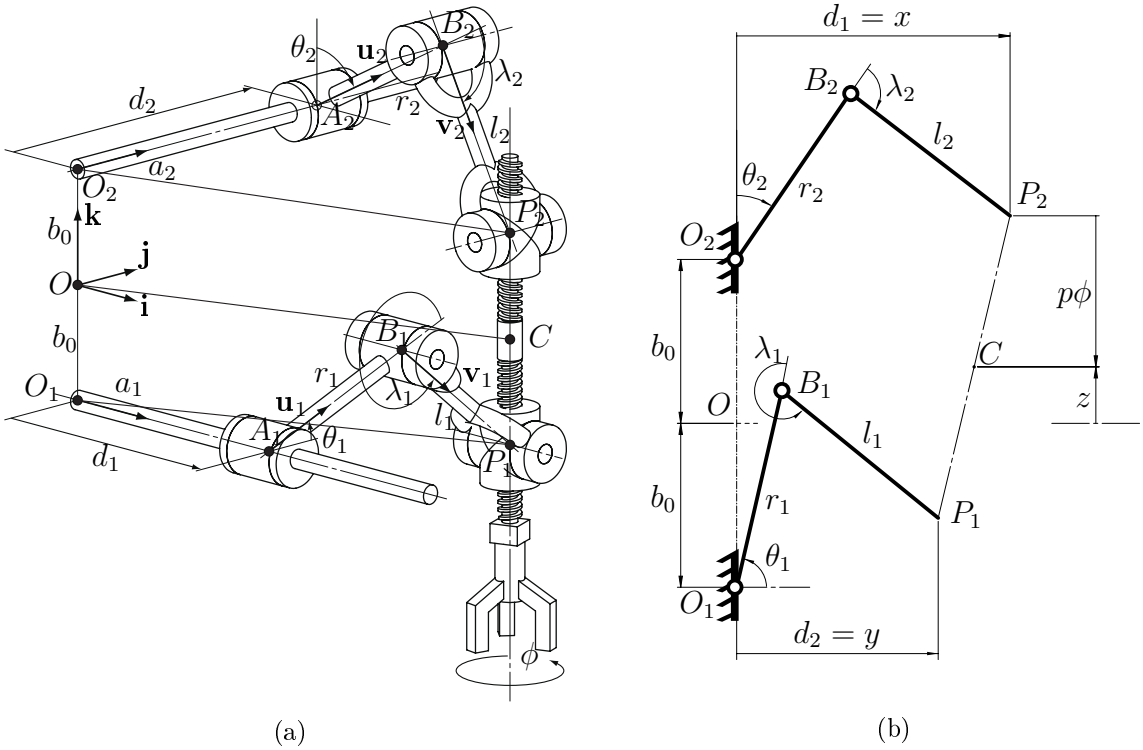


Figure 2–3: Schematic representations of the PMC: (a) 3D model; and (b) planar diagram of the PMC at an arbitrary posture

## 2.4 Displacement Analyses of the PMC

The forward and inverse displacement analyses of the PMC are available [19, 20, 21], and briefly recalled here for quick reference, while new results, on the possible assembly modes, are reported. The PMC admits four possible postures for one given PM pose, and four PM poses for a given pair of actuated-joint variable values.

### 2.4.1 Inverse Displacement Analysis

The Inverse Displacement Analysis (IDA) determines the displacements of the actuated C-joints from the pose—position ($x$, $y$, $z$) and orientation ($\phi$)—of the PM. The $x$- and $y$-coordinates of the PM lead directly to the C-joint translation variables

$d_1$ and $d_2$:

$$d_1 = x, \quad d_2 = y \tag{2.8}$$

From previous results, the C-joint angular displacements $\theta_1$ and $\theta_2$ are the solutions of the relation

$$(\mathbf{q}_i^T \mathbf{x}_i) \cos\theta_i + (\mathbf{q}_i^T \mathbf{y}_i) \sin\theta_i = \frac{\mathbf{q}_i^T \mathbf{q}_i + r_i^2 - l_i^2}{2r_i} \tag{2.9}$$

with

$$\mathbf{x}_1 \equiv \mathbf{j}, \quad \mathbf{x}_2 \equiv \mathbf{k}, \quad \mathbf{y}_1 \equiv \mathbf{k}, \quad \mathbf{y}_2 \equiv \mathbf{i} \tag{2.10a}$$

$$\mathbf{q}_1 \equiv \begin{bmatrix} x - d_1 \\ y \\ z - b_0 + p\phi \end{bmatrix}, \quad \mathbf{q}_2 \equiv \begin{bmatrix} x \\ y - d_2 \\ z + b_0 - p\phi \end{bmatrix} \tag{2.10b}$$

where the unit vectors $\mathbf{i}$, $\mathbf{j}$ and $\mathbf{k}$ and length $b_0$ are defined in Fig. 2–3a. Relation (2.9) is solved by introduction of the well-known *tan-half identities*:

$$\cos\theta_i \equiv \frac{1 - T_i^2}{1 + T_i^2}, \quad \cos\theta_i \equiv \frac{2T_i}{1 + T_i^2}, \quad T_i \equiv \tan\frac{\theta_i}{2} \tag{2.11}$$

Relation (2.9) is thus recast as

$$A_i \frac{1 - T_i^2}{1 + T_i^2} + B_i \frac{2T_i}{1 + T_i^2} + C_i = 0 \tag{2.12a}$$

where

$$A_i \equiv \mathbf{q}_i^T \mathbf{x}_i, \quad B_i \equiv \mathbf{q}_i^T \mathbf{y}_i, \quad C_i \equiv -\frac{\mathbf{q}_i^T \mathbf{q}_i + r_i^2 - l_i^2}{2r_i} \tag{2.12b}$$

Equation (2.12a) is readily rearranged as a quadratic polynomial in $T_i$

$$(C_i - A_i) T_i^2 + 2B_i T_i + C_i + A_i = 0 \tag{2.12c}$$

Table 2–1: Correspondence between $j$ and inverse/forward conjugate postures

| Limb Index | Elbow-down/Forearm-up | Elbow-up/Forearm-down |
|---|---|---|
| $i = 1$ | $j = 2$ | $j = 1$ |
| $i = 2$ | $j = 1$ | $j = 2$ |

whose roots are

$$T_{ij} = \frac{-B_i \mp \sqrt{A_i^2 + B_i^2 - C_i^2}}{C_i - A_i}, \quad j = 1,\, 2 \tag{2.12d}$$

The solutions for $\theta_i$ are computed from the roots $T_{ij}$, $j = 1,\, 2$, and denoted $\theta_{ij}$:

$$\theta_{ij} = 2 \arctan\left(-B_i + (-1)^j \sqrt{A_i^2 + B_i^2 - C_i^2},\quad C_i - A_i\right) \tag{2.12e}$$

where $\arctan(\cdot,\, \cdot)$ is the four-quadrant `arctangent` function. For a given limb $i$, the two angles $\theta_{ij}$ correspond to the solutions for the two possible limb postures[1]; each limb $i$ can be oriented with the "elbow" between the proximal and distal links pointing either up or down with respect to the horizontal, called the *elbow-up* and *elbow-down* inverse conjugate postures (ICP), respectively. The correspondence between $j$ and the limb posture is given in Table 2–1. Figure 2–3a shows an up-up inverse kinematic posture, while an elbow-down inverse kinematic posture is illustrated by limb 1 in Fig. 2–4b

[1] $\theta_{i1}$ and $\theta_{i2}$ are equal when the proximal and distal link of the $i^{th}$ limb are parallel.

**Solution of the IDA for the Prototype**

For the prototype, $\theta_1$ and $\theta_2$ take the values $\theta_{11}$ and $\theta_{22}$, respectively. Plugging in the design specification from eq.(2.7) yields the closed-form solutions

$$\theta_1 = 2\arctan\left(-P_{1z} - \frac{1}{2}\sqrt{4y^2 + 4P_{1z}^2 - \frac{\left(y^2 + P_{1z}^2\right)^2}{r^2}}, \quad -\frac{y^2 + P_{1z}^2}{2r} - y\right) \tag{2.13a}$$

$$\theta_2 = 2\arctan\left(-x + \frac{1}{2}\sqrt{4x^2 + 4P_{2z}^2 - \frac{\left(x^2 + P_{2z}^2\right)^2}{r^2}}, \quad -\frac{x^2 + P_{2z}^2}{2r} - P_{2z}\right) \tag{2.13b}$$

where $P_{1z}$ and $P_{2z}$ are the $z$-coordinates of points $P_1$ and $P_2$ from Fig. 2–3a, namely

$$P_{1z} \equiv z + b_0 + p\phi, \quad P_{2z} \equiv z - b_0 - p\phi \tag{2.13c}$$

The solution of the IDA is provided directly by eqs.(2.8) and (2.13a–2.13b), without the need to select between multiple solutions. By virtue of its computational simplicity, the IDA is readily performed in real-time by a digital control system. As the foregoing analysis employs the conventional solutions to quadratic equations, the expressions for $\theta_i$ may produce unwanted results due to *catastrophic cancellations*, and other pitfalls identified by Forsythe [33]. Robust algorithms for the solution of quadratic equations could be employed, but this is not necessary as long as the PMC is operated within the reachable workspace, to be derived in Section 2.5.3.

### 2.4.2 Forward Displacement Analysis

The FDA produces the PM displacements from the C-joint displacements. Translational PM coordinates $x$ and $y$ are obtained directly from $d_1$ and $d_2$ as in eq.(2.8).

Manipulating earlier results [21] yields expressions for $z$ and $\phi$, namely

$$\begin{bmatrix} z \\ \phi \end{bmatrix} = \frac{1}{2p} \begin{bmatrix} p\,(r_2 \cos\theta_2 + l_2 c_2 + r_1 \sin\theta_1 + l_1 s_1) \\ r_1 \sin\theta_1 + l_1 s_1 - r_2 \cos\theta_2 - l_2 c_2 - 2b_0 \end{bmatrix} \tag{2.14a}$$

$$s_i \equiv \sin(\theta_i + \lambda_i), \quad c_i \equiv \cos(\theta_i + \lambda_i), \quad i = 1,\, 2 \tag{2.14b}$$

Introducing the design specifications from eq.(2.7), the foregoing expressions become

$$\begin{bmatrix} z \\ \phi \end{bmatrix} = \frac{r}{2p} \begin{bmatrix} p\,(\sin\theta_1 + s_1 + \cos\theta_2 + c_2) \\ \sin\theta_1 + s_1 - \cos\theta_2 - c_2 - 2b_0/r \end{bmatrix} \tag{2.15}$$

The term $b_0$ vanishes in the expression for $z$, and does not appear in those for $x$ and $y$. From a kinematics standpoint, only the orientation $\phi$ of the PM is influenced by the choice of $b_0$, or, more precisely, by the ratio $b_0/r$, which offsets the orientation.

Variables $z$ and $\phi$ admit four possible solutions, corresponding to the four *forward-kinematics branches* of the mechanism, as each distal link can be pointed "up" or "down"; these are therefore called *forearm-up* and *forearm-down* forward conjugate postures (FCP). A quadruple of postures is shown in Fig. 2–4a, and two of the resulting PM positions are indicated by points $C$ and $C'$.

Revisiting the definitions of $s_i$ and $c_i$ in eq.(2.14b) and earlier results [21], the values of angles $\lambda_i$—the angle of the "elbow" between the proximal and distal links—are obtained from the solutions of

$$r_1 \cos\theta_1 + l_1 \cos(\theta_1 + \lambda_1) = y \tag{2.16a}$$

$$r_2 \sin\theta_2 + l_2 \sin(\theta_2 + \lambda_2) = x \tag{2.16b}$$

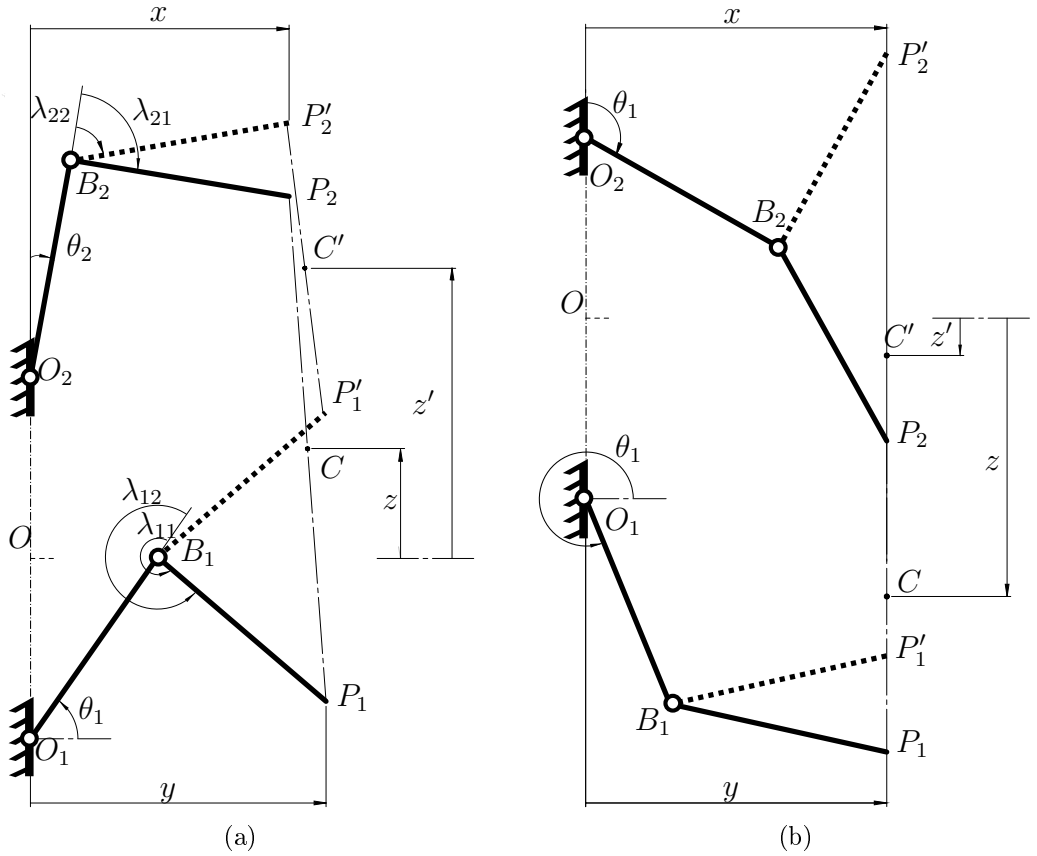


Figure 2–4: Forward and inverse conjugate postures: (a) Down-down (solid line) and up-up (dotted line) FCP; and (b) elbow-down (both postures of limb 1, "dotted" posture of limb 2) and elbow-up ("solid" posture of limb 2) ICP, with $x = y = d_i^{max}$

leading to pairs of solutions for $\lambda_i$, denoted $\lambda_{ij}$, namely,

$$\lambda_{11} = -\arccos\left(\frac{d_2 - r_1\cos\theta_1}{l_1}\right) - \theta_1 \tag{2.17a}$$

$$\lambda_{12} = \arccos\left(\frac{d_2 - r_1\cos\theta_1}{l_1}\right) - \theta_1 \tag{2.17b}$$

$$\lambda_{21} = \arcsin\left(\frac{d_1 - r_2\sin\theta_2}{l_2}\right) - \theta_2 \tag{2.17c}$$

$$\lambda_{22} = -\arcsin\left(\frac{d_1 - r_2\sin\theta_2}{l_2}\right) - \theta_2 + \pi \tag{2.17d}$$

The meaning of subscript $j$ in $\lambda_{ij}$ is given in Table 2–1; therefore, solutions $\lambda_{11}$ and $\lambda_{22}$ produce the correct values of $\lambda_1$ and $\lambda_2$, respectively, for the down-down forward-kinematics branch. The FDA is concluded upon plugging eqs.(2.17a & 2.17d) into eq.(2.14b) and solving eq.(2.15) for $z$ and $\phi$. Explicit solutions are given in the right-hand side of eqs.(2.27 & 2.28d).

## 2.5 Mobility Analysis of the PMC

Analyses of the reachable workspace—the volume that the PM can reach in at least one orientation [34]—and the rotatability—the rotational mobility of the PM within the workspace—were reported by P.-C. Lee and J.-J. Lee [17] using an arbitrary architecture for the PMC. Further analyses are now conducted with the architecture of the PMC prototype, taking into account the forward-kinematics branches.

### 2.5.1 Workspace Analysis

The reachable workspace analysis cited above led to maximum and minimum C-joint displacements, and to the workspace by plugging these values directly into the FDA. Consequently, the workspace contained singularities and branch switching. An equivalent analysis is not included here for conciseness. Instead, a safe operating workspace of the PMC prototype is derived. As indicated by Fig. 2–4b, forward- and inverse-kinematics branches are different but intersecting. The PM is restricted to the region of intersection of the down-down forward-kinematics branch (forearm-down) and the up-up inverse-kinematics branch (elbow-up). New bounds on C-joint displacements are now derived, yielding practical parameters for safe robot operation.

### C-joint Displacement Constraints

The translational variables of the C-joint are constrained by the stroke of the C-drive prototype ballscrews and the layout of the drives. In the prototype layout, the bounds are:

$$d_i^{min} = 191\,\text{mm}, \quad d_i^{max} = 407\,\text{mm}, \quad i = 1,\, 2 \tag{2.18}$$

where $d_i^{min}$ and $d_i^{max}$ are the minimum and maximum C-joint translations, respectively. The C-joint stroke length is therefore 216 mm. Furthermore, the rotational constraints of the C-joint are

$$\theta^{min} \equiv \theta_1^{min} = -\theta_2^{min} + \pi/2, \quad \theta^{max} \equiv \theta_1^{max} = -\theta_2^{max} + \pi/2 \tag{2.19}$$

where $\theta^{min}$ and $\theta^{max}$ are the minimum and maximum rotational displacements of the C-joints, following the definition of angle $\theta_1$. The equivalent bounds for the second C-joint, namely $\theta_2^{min}$ and $\theta_2^{max}$, are obtained from the foregoing relation. The numerical values of these constraints are discussed below.

### PM Ballscrew Displacement Constraints

The two ballscrews of the PM have a pitch of 20 mm and a usable stroke length of approximately 45 mm. The PM is therefore capable of performing two full turns. From the FDA, the orientation $\phi$ of the PM in the middle of its range of rotation is

$$\phi_{centre} = -\frac{122}{5}\pi \tag{2.20a}$$

while the bounds of the range are

$$\phi_{max} = -\frac{112}{5}\pi, \quad \phi_{min} = -\frac{132}{5}\pi \tag{2.20b}$$

and hence, the range of rotation $\Delta\phi$ is

$$\Delta\phi = \phi_{max} - \phi_{min} = \frac{20}{5}\pi = 4\pi \tag{2.21}$$

which is exactly two turns.

**Maximum Vertical Displacement**

The maximum vertical displacement of the PMC is obtained for every $xy$–position when both C-joints are at their maximum displacement $\theta_i^{max}$, $i = 1, 2$. Beyond these angles, the PMC approaches a singular posture in which one or both distal links are horizontal, as shown in Fig. 2–5a.

The maximum safe displacement $\theta^{max}$ is therefore bounded by the angle giving rise to these singular postures, which is denoted $\theta_s^{max}$ at its minimum value, that is, when the arms are "fully extended" at $x = y = d_i^{max}$. The angle $\theta_s^{max}$ is found to be

$$\theta_s^{max} = 1.21 \text{ rad} \approx 69.1^\circ \tag{2.22}$$

leading to angles $\theta_{1s}^{max}$ and $\theta_{2s}^{max}$ for the first and second limb, respectively, obtained via the same relations as eq.(2.19). A margin of safety is introduced by the requirement that the distal links always be oriented at greater than or equal to 30° with respect to the horizontal plane. Amending the foregoing calculation, the maximum safe C-joint displacement $\theta^{max}$ that avoids singularities for every $xy$–position is

$$\theta^{max} = 1.058 \text{ rad} \approx 60^\circ, \qquad \theta^{max} < \theta_s^{max} \tag{2.23}$$

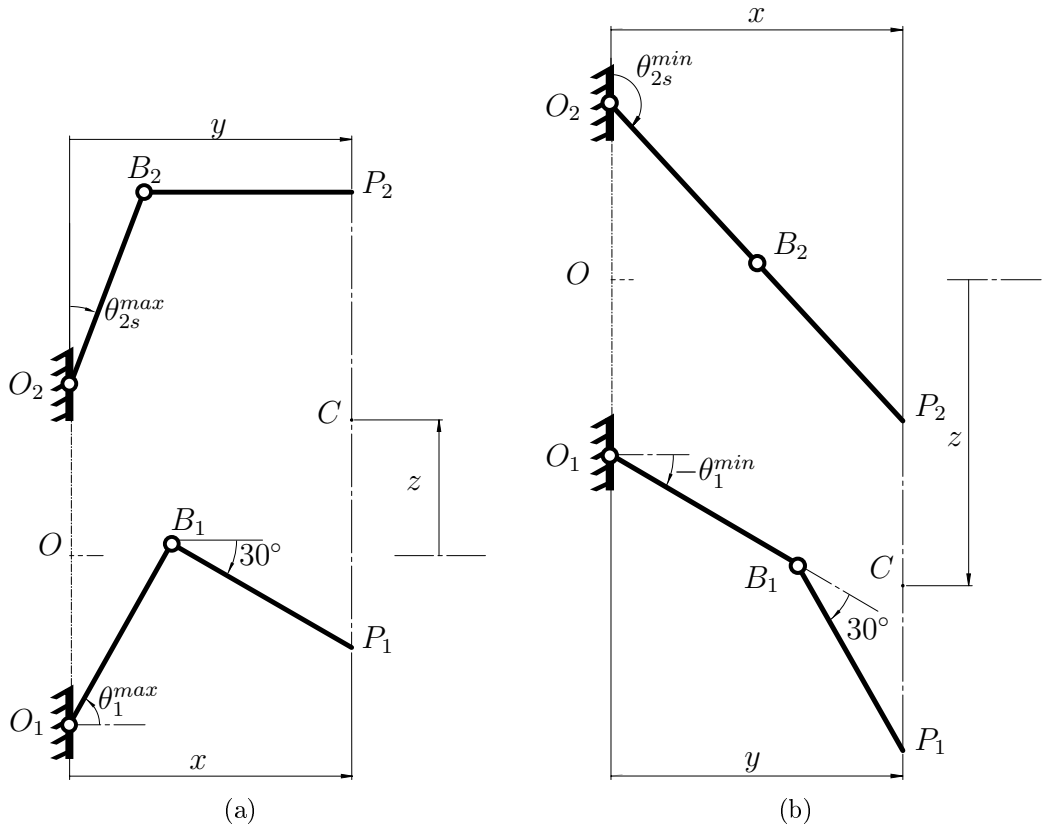


Figure 2–5: PMC postures with $x = y = d_i^{max}$: (a) Limb 1 with $\theta_1 = \theta_1^{max}$ and limb 2 with $\theta_2 = \theta_{2s}^{max}$ illustrate a safe posture and a singular posture, respectively; and (b) the same, for limb 1 with $\theta_1 = \theta_1^{min}$ and limb 2 with $\theta_2 = \theta_{2s}^{min}$

The upper limit of the workspace is then readily computed by plugging the foregoing result into eq.(2.13b) and the first row of eq.(2.15), as plotted in Fig. 2–6a. The stroke length of the PM ballscrews is not taken into account in these renderings.

**Minimum Vertical Displacement**

As with the computation of the maximum vertical displacement of the PM, the motion of the PMC is limited at the bottom of its workspace by a singularity, namely when the proximal and distal links become parallel. The minimum vertical

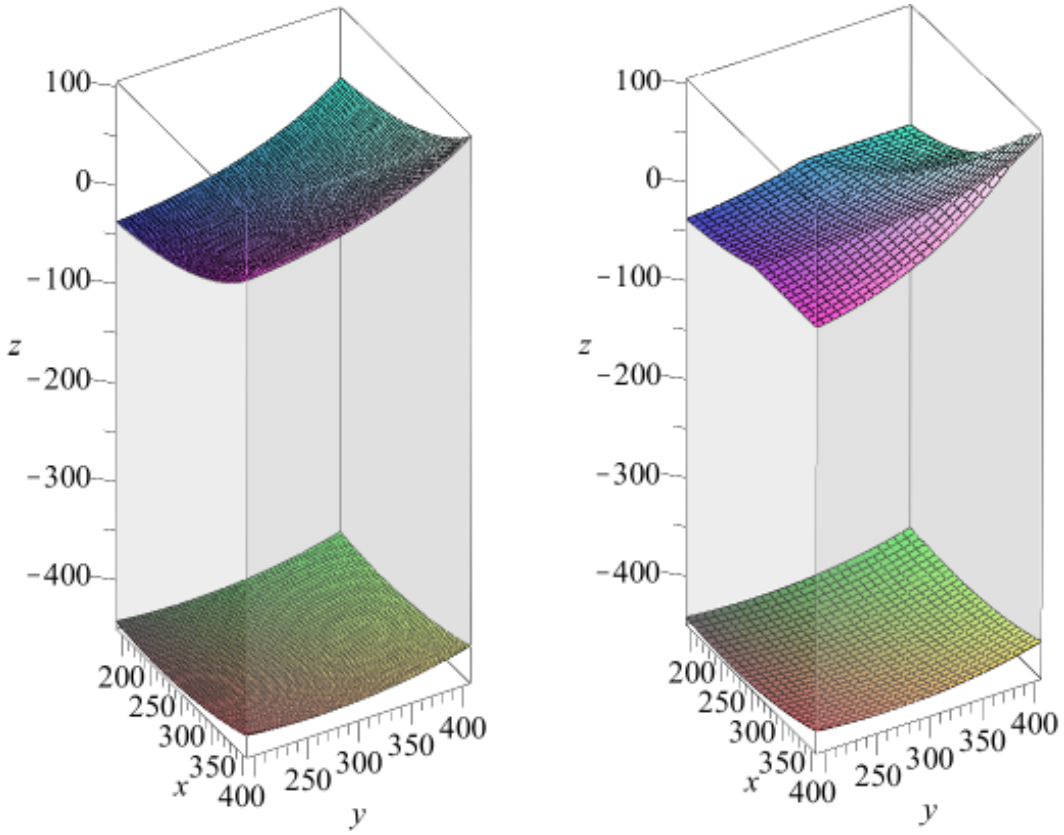


Figure 2–6: Reachable workspace (shaded volume): (a) With unbounded PM screw stroke; and (b) with bounded PM screw stroke

displacement of the PMC is obtained for every $xy$–position when both C-joints are at their minimum displacements $\theta_i^{min}$. Beyond these angles, the PMC approaches the aforementioned singular posture, as shown for limb 2 in Fig. 2–5b. The minimum safe displacement $\theta^{min}$ is therefore bounded by the angle giving rise to these singular postures, which is denoted $\theta_s^{min}$ at its maximum value, that is, when the limbs are "fully extended" at $x = y = d_i^{max}$. Angle $\theta_s^{min}$ is readily computed from

eqs.(2.16a & 2.16b) by plugging in $\lambda_1 = \pi$ and $\lambda_2 = 0$, thereby obtaining

$$\theta_s^{min} = -0.825\,\text{rad} \approx -47^\circ \tag{2.24}$$

which leads, as earlier, to angles $\theta_{1s}^{min}$ and $\theta_{2s}^{min}$ for limbs 1 and 2, respectively. A margin of safety is introduced by the requirement that the directions of the distal links always be at least 30° from parallel, the limit case happening when

$$\lambda_1 = -30^\circ, \quad \lambda_2 = 30^\circ \tag{2.25a}$$

which leads to the bound

$$\theta^{min} = -.530\,\text{rad} \approx -30^\circ, \qquad \theta^{min} > \theta_s^{min} \tag{2.25b}$$

and thus to angles $\theta_1^{min}$ and $\theta_2^{min}$. The lower bound of the workspace is then readily computed by plugging the foregoing results into eq.(2.13b) and the first row of eq.(2.15), as plotted in Fig. 2–6a.

### 2.5.2 Rotatability Analysis

The extrema of the PM rotational mobility throughout the workspace—neglecting the stroke length of the PM screws—are readily computed by plugging the extreme angular displacements of the C-joints from eqs.(2.23 & 2.25b) into the FDA. The maximum angle of rotation of the PM is obtained by setting

$$\theta_1 = \theta_1^{max}, \quad \theta_2 = \theta_2^{min} \tag{2.26a}$$

while the minimum value of $\phi$ is obtained from

$$\theta_1 = \theta_1^{min}, \quad \theta_2 = \theta_2^{max} \tag{2.26b}$$

The resulting plots are shown in Figs. 2–7. The transparent parallelepiped represents

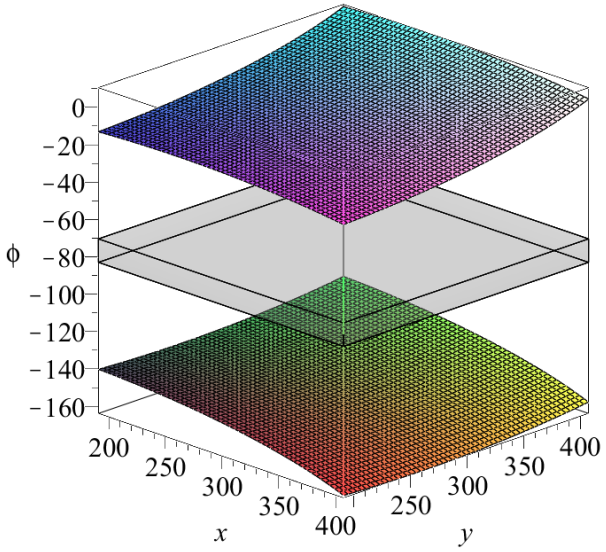


Figure 2–7: PMC rotatability

the range of rotation of the PM prototype, namely two full turns. Positive values for $\phi$ can never occur, as the two screws would overlap.

### 2.5.3 Prototype Reachable Workspace

The stroke lengths of the PM ballscrews are now considered in order to obtain the true reachable workspace of the prototype. The maximim and minimum $z$ that can be reached at every $xy$–position are found through optimization. The objective function, denoted $z_{obj}(d_1,\, d_2,\, \theta_1,\, \theta_2)$, is the first component of eq.(2.14a) from the FDA, namely

$$z_{obj}(d_1,\, d_2\, \theta_1,\, \theta_2) \equiv \frac{r}{2}\Bigg( \sin\theta_1 - \sqrt{1 - \frac{(d_2 - r\cos\theta_1)^2}{r^2}} + \cos\theta_2 \\ -\sqrt{1 - \frac{(d_1 - r\sin\theta_2)^2}{r^2}}\Bigg) \tag{2.27}$$

The objective function is maximized and minimized under nonlinear inequality constraints:

$$\theta_1^{min} \leq \text{wrap}(\theta_1) \leq \theta_1^{max}, \quad \theta_2^{min} \leq \text{wrap}(\theta_1) \leq \theta_2^{max} \tag{2.28a}$$

$$\phi_{min} \leq \phi(d_1,\, d_2,\, \theta_1,\, \theta_2) \leq \phi_{max} \tag{2.28b}$$

where the wrap$(\cdot)$ function that recasts its argument to lie between $-\pi$ and $\pi$ is

$$\text{wrap}(\cdot) \equiv \arctan(\sin(\cdot),\, \cos(\cdot)) \tag{2.28c}$$

and $\phi_{obj}(d_1,\, d_2,\, \theta_1,\, \theta_2)$ is obtained from the second row of eq.(2.14a), namely

$$\phi_{obj}(d_1,\, d_2,\, \theta_1,\, \theta_2) \equiv \frac{r}{2p}\left( \sin\theta_1 - \sqrt{1 - \frac{(d_2 - r\cos\theta_1)^2}{r^2}} - \cos\theta_2 \right. \\ \left. + \sqrt{1 - \frac{(d_1 - r\sin\theta_2)^2}{r^2}} - \frac{2b_0}{r} \right) \tag{2.28d}$$

A sequential quadratic programming algorithm is implemented in Maple to solve this optimization problem with non-linear inequality constraints, using the `NLPSolve()` function from the `Optimization` package. Choosing feasible values for $\theta_i$ as initial guesses, the upper and lower bounds of the reachable workspace are computed and plotted in Fig. 2–6b.

# CHAPTER 3
# Detailed Design of the PMC

## 3.1 Hardware Available at the RMSLab

The McGill SMG, shown in Fig. 1–3a, was located at the RMSLab of the Centre for Intelligent Machines (CIM). The robot was dismantled, and several components reused for the PMC, to save time and funds. The main repurposed components are:

1. The metal frame and protective acrylic shields.
2. The servomotors and amplifiers, the control box, the control computers.
3. Carbon fibre tube assemblies, to be used as the PMC distal links.

The full description of these components was reported by Angeles et al. [35].

## 3.2 General Dimensions of the PMC

Initial conceptual design work on the PMC was performed by Damien Trézières et al. [28]. Subsequent detailed design work was built upon those efforts.

In order to carry out the industry standard pick-and-place motion, the PMC must be capable of performing 300 mm translation in the $xy$-plane and 25 mm translation in the $z$ direction. The square $xy$ workspace of the PMC is shown in Fig. 3–1. The diagonal length of the square is 300 mm, the sides being therefore approximately 212 mm. The minimum allowable translational capability of the C-drives must therefore be 212 mm.

While the carbon fibre tube assemblies from the McGill SMG are used as the distal links of the PMC, the proximal links are given the same length to simplify

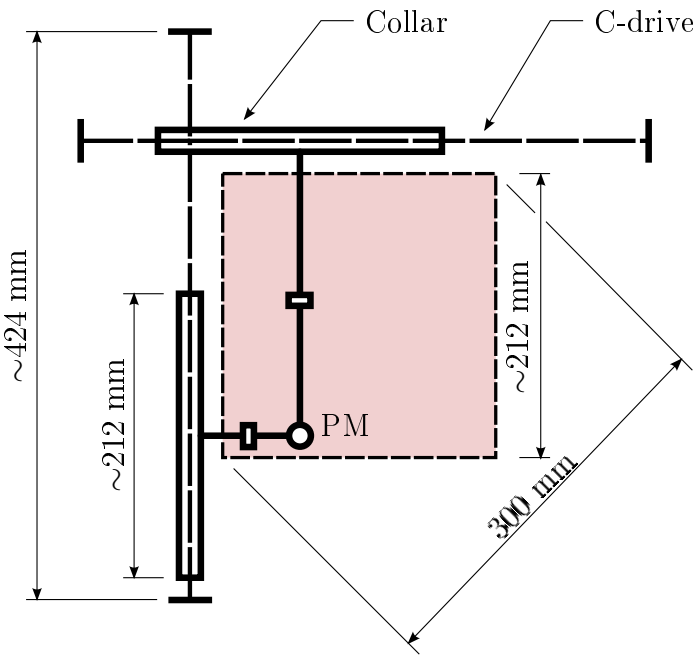


Figure 3–1: Schematic top view of the PMC. The $xy$ workspace of the PM is represented by the shaded square.

the design and analysis. Recalling the nomenclature from Fig. 2–3a, the link lengths become

$$r \equiv r_1 = r_2 = l_1 = l_2 = 300\,\text{mm} \tag{3.1}$$

Length $b_0$, a key geometric parameter, is illustrated in Fig. 2–3a. Given the space constraints of the existing robot frame, a convenient value was found to be

$$b_0 = 244\,\text{mm} \tag{3.2}$$

The spacing between the C-drives is readily changed on the PMC prototype. The dimensions $r$ and $b_0$ fully determine the architecture and kinematics of the PMC, and are the only design parameters to appear in the displacement analyses in Section 2.4.

### 3.2.1 General Dimensions of the C-drive

The principal dimensions of the C-drive are represented schematically in Fig. 3–2. The translational mobility of the C-drive is referred to as its *stroke*. Ballscrews are conventionally dimensioned by their *nominal stroke*, which does not include the width of the ballnuts. The following relationships hold:

$$\text{Usable stroke} \equiv \text{Nominal stroke} - \text{Ballnut width} \tag{3.3a}$$

$$\text{Inner collar} = \text{Usable stroke} + \text{Gap} \tag{3.3b}$$

When the foregoing expression is respected, then

$$\text{C-drive stroke} = \text{Usable stroke} \tag{3.3c}$$

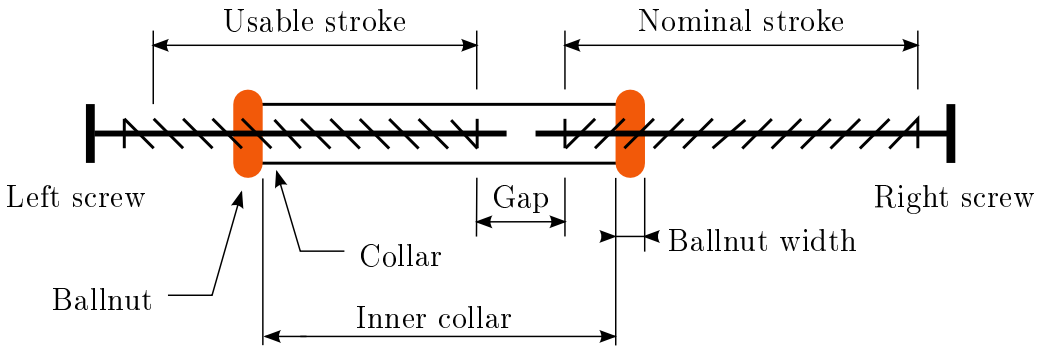


Figure 3–2: Schematic of the C-drive, indicating principal dimensions

The C-drives are therefore designed with a stroke of 216 mm, incorporating a 4 mm margin.

### 3.2.2 General Dimensions of the PM

As many industrial parallel robots are limited to half a turn, a maximum rotatability of two full turns is selected to demonstrate the superior capabilities of the PMC. The choice of screw pitch is constrained by the availability of ballscrews with

both left- and right-handed threads, as well as by the corresponding screw diameters, which tend to increase with the pitch, thereby increasing the screw weight. Ballscrews with a pitch and diameter of 20 mm are selected[1]:

$$p = p_1 = -p_2 = \frac{20}{2\pi} \tag{3.4}$$

A usable stroke length of 45 mm is chosen, allowing for up to 2.25 full turns of the PM, leaving a 0.25 turn safety margin. The centrepoints of the usable stroke of the screws are denoted $M_1$ and $M_2$. Figure 3–3 shows the principal parts and dimensions of the PM.

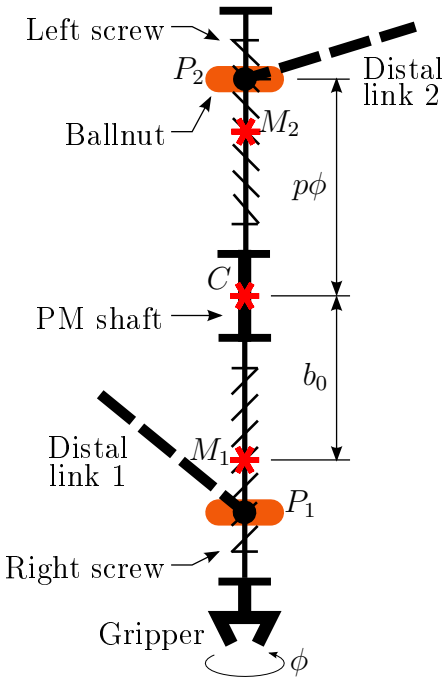


Figure 3–3: Schematic of the PM. The top and bottom screws are left- and right-handed, respectively.

Point $C$ is the centre of the PM, equidistant to points $M_1$ and $M_2$, while points $P_1$ and $P_2$ are the centres of the threaded U-joints of the lower and upper wrists, respectively. The distances $CP_1$ and $CP_2$ are equal to $p\phi$. The concept of *isotropic posture* is now introduced, referring to a posture of the PMC at which its Jacobian matrices are isotropic. Only one such posture arises within the kinematics branches in which the PMC operates. This posture is shown in Fig. 3–4.

[1] It is necessary to divide the pitch length by $2\pi$ for consistency with a previous study [21].

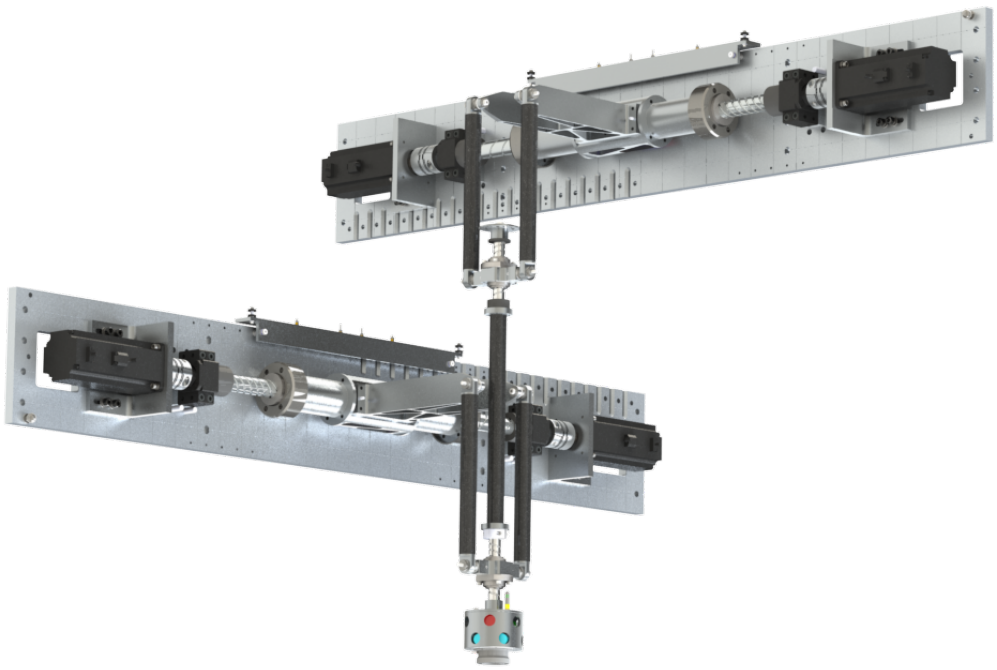

Figure 3–4: 3D CAD rendering of the PMC in its isotropic posture

By design, the isotropic posture occurs when the PM is centred, that is, when points $P_1$ and $P_2$ coincide with points $M_1$ and $M_2$, respectively. This is verified when

$$CM_1 = CM_2 = b_0 \quad \Leftrightarrow \quad M_1M_2 = 2b_0 \tag{3.5}$$

The length of the PM shaft connecting the two screws is chosen accordingly.

### 3.3 Detailed Design of the PMC Prototype

The detailed design of a single limb of the PMC is illustrated in the CAD model in Fig. 3–5, while Fig. 3–6 is a picture of the full prototype. Important aspects of the design of the limbs are now summarized.

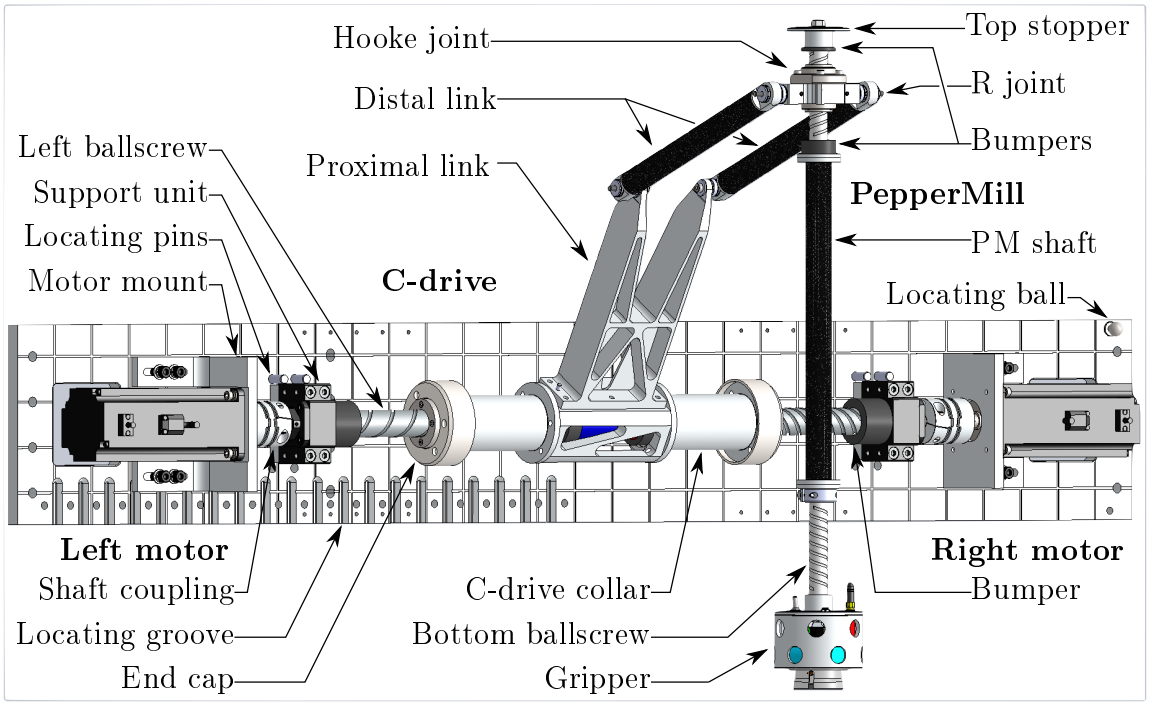


Figure 3–5: Whole upper limb

### 3.3.1 Proximal Link

The proximal link is composed of the C-drive collar and the proximal link fork, which is machined out of a single piece of aluminum. The fork shape of the latter prevents mechanical interference with the PM shaft throughout the entire reachable workspace of the PMC.

### 3.3.2 Distal Link

The distal link is embodied by two identical carbon fibre tubes with aluminum inserts in which are mounted needle-roller bearings. The space between the tubes leaves clearance for the PM shaft. They are mounted on the outside of the proximal

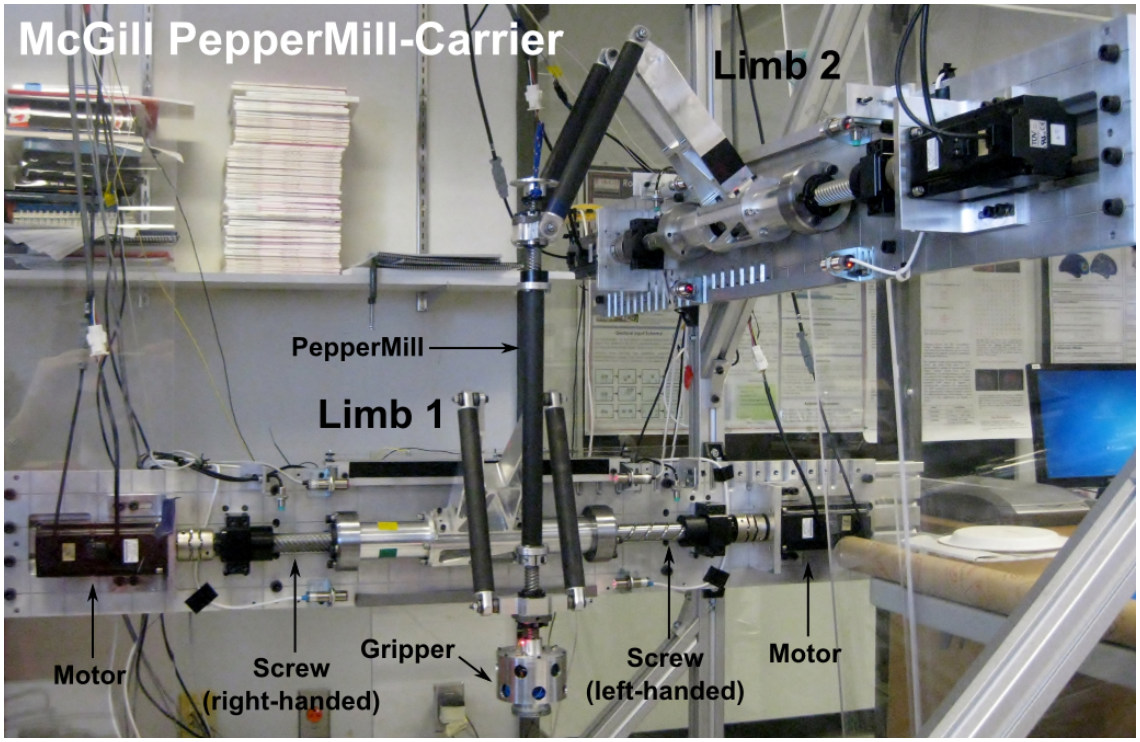


Figure 3–6: Complete collar

link to avoid mechanical interference throughout the entire reachable workspace of the PMC.

The links are reused from the original McGill SMG prototype [35]. The revolute joint between the proximal and distal links is embodied by two coaxial joints, of which one is shown in Fig 3–7. The assembly is held together by a nut and Belleville washers, not shown on the figure. The number and arrangement of these washers, as well as the nut tightening torque, determine the joint friction and compliance.

### 3.3.3 The Hooke Joint

The link connecting the distal link to the PM is called a Hooke joint, as shown in Fig. 3–8. The body of the Hooke joint is machined out of a single piece of aluminum.

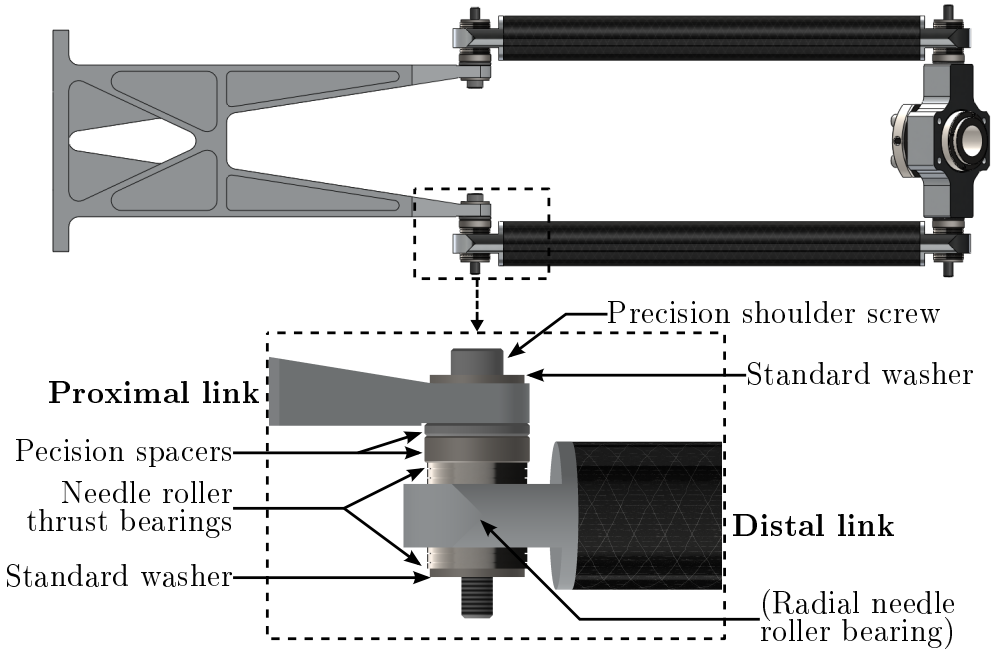


Figure 3–7: Side view of joint between proximal and distal links

The bearing arrangement is the same as in Fig. 3–7, except that the precision shoulder screw is substituted for a precision shaft that has one end threaded and the other grooved to accommodate set-screws.

### 3.3.4 PM

The PM two helical joints are back-driven by the translation of the nuts in order to rotate the gripper. They are therefore embodied by ballscrews rather than lead screws, by virtue of their higher back-driving efficiency, superior accuracy and lower backlash. The PM thus comprises three main components: two ballscrews and a lightweight PM shaft. The latter is constructed from a carbon fibre tube with a flanged aluminum insert adhered to each end. The ballscrews are fixed to the other components by means of their threaded ends.

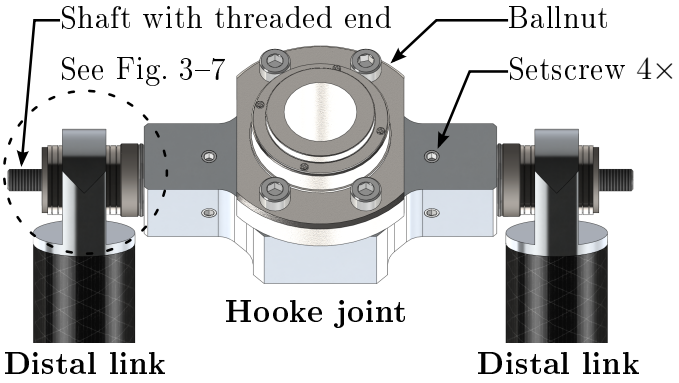


Figure 3–8: Descriptive view the Hooke joint between distal link and PM. The ballscrew is hidden for clarity

### 3.4 Detailed Design of the C-drive

Each C-drive is built on a base machined from a single plate of high-precision cast aluminum. This material exhibits low warping when machined compared to conventional rolled aluminum sheets, allowing for accurate assembly of the C-drive. The motors are fixed on the base via adjustable mounts, as shown in Fig. 3–10. Each ballscrew is mounted on the base by a support unit containing a pair of angular contact ball bearings, which bear both axial and radial loads. The ballscrews are joined at their free ends by a custom coupling containing a radial needle-roller bearing, as shown in Fig. 3–11. This coupling supports only radial forces, and tolerates small axial translations between the ballscrews.

### 3.5 Design of the Collar Middle Part for Testing

The mass driven by each C-drive of the PMC is constant—computed in CAD—and equal to half of the robot mass. By virtue of the robot symmetry, the load is

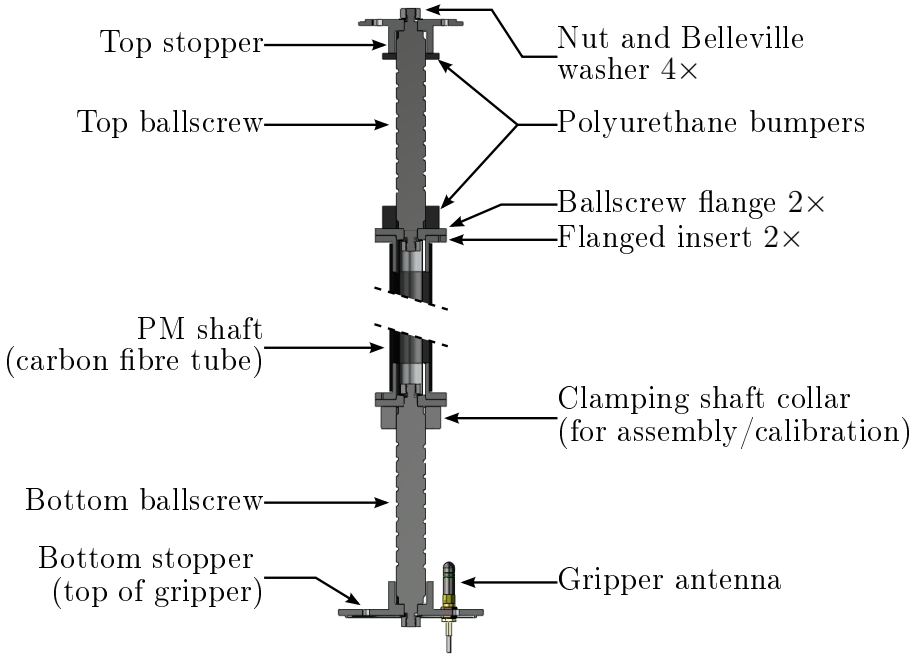


Figure 3–9: Cross section view of the PM, with the gripper and ballnuts hidden

shared evenly between the two C-drives. The moment of inertia about each C-drive axis is posture-dependent.

The C-drives are first tested independent of the PMC in order to collect data on their performance and tune the controller before robot assembly. For testing purposes, the collar should ideally carry half the inertia load of the assembled robot. The collar is composed of three parts, the middle and the two ends, as shown in Fig. 3–12. The lightweight collar middle part, shown in Fig. 3–10, is designed to be connected to the proximal link fork. A heavy steel tubular middle part is substituted for C-drive testing. Using CAD software, the desired mass $m_M$ of the middle part,

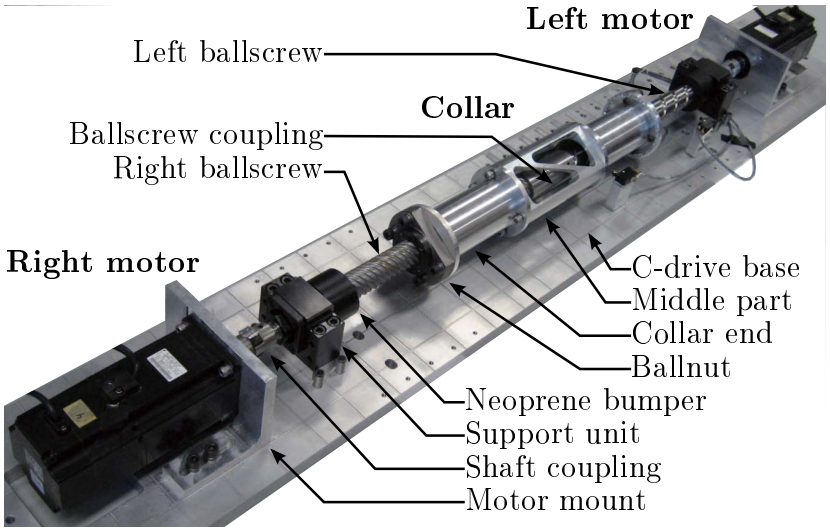


Figure 3–10: Annotated picture of the C-drive

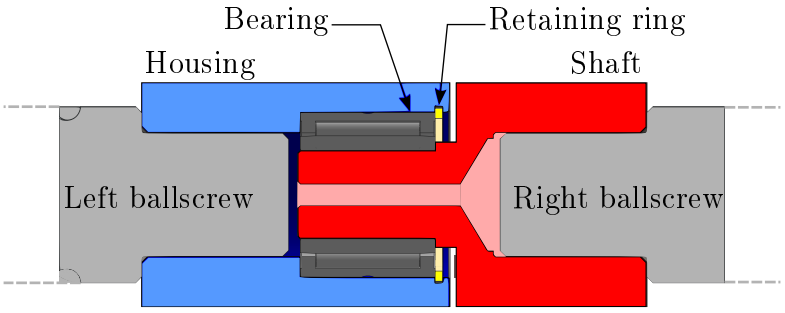


Figure 3–11: Ballscrew coupling: bearing, housing and shaft

namely approximately half of the PMC mass, is obtained as

$$m_M = 3279\,\mathrm{g} \tag{3.6}$$

The resulting dimensions of the outer and inner radii of the collar middle part, $r_1$ and $r_2$ respectively, are rounded up to convenient values and become

$$r_1 = 44.5\,\mathrm{mm}, \quad \mathrm{r}_2 = 30\,\mathrm{mm} \tag{3.7}$$

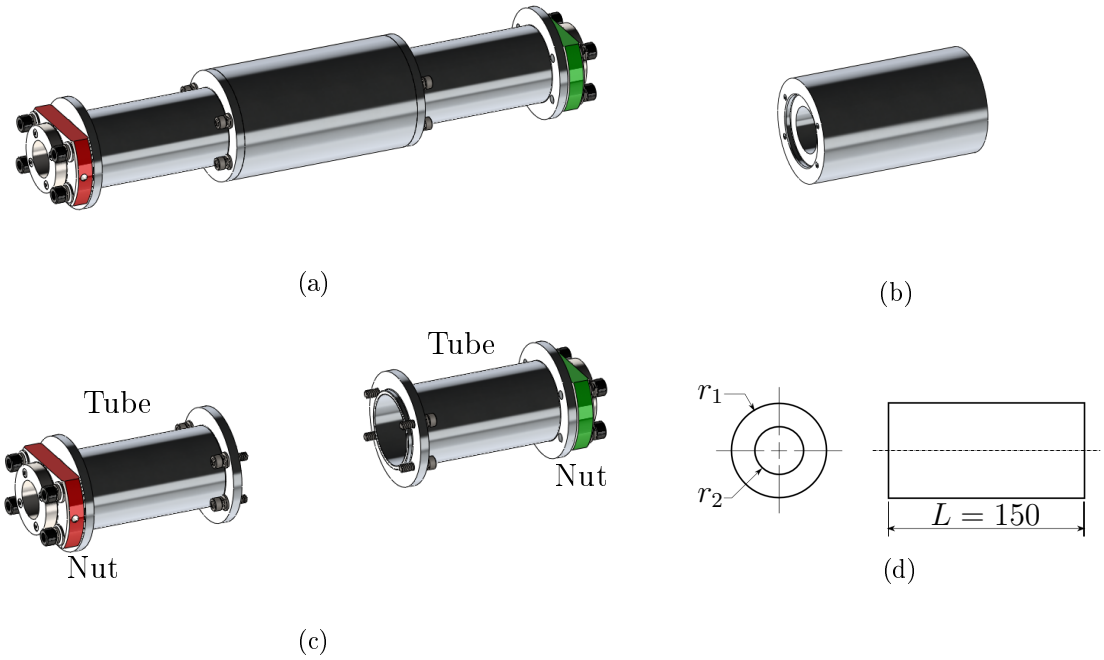


Figure 3–12: Collar components (end caps not shown): (a) Complete collar; (b) middle part; (c) ends; and (d) dimensions of the middle part, subject to $r_2 > 15\,\text{mm}$

The collar is statically and dynamically balanced by virtue of its symmetries. As space constraints prevent the C-drive from being designed with the same moment of inertia as a PMC limb, the C-drive tests cannot faithfully replicate the operation of the PMC when the drives rotate. However, these tests provide insight into the feasibility of the C-drive to actuate the PMC.

# CHAPTER 4
# Control: Modelling and Implementation

## 4.1 Control System Setup

### 4.1.1 Overview of Prototype Control

The prototype features a digital control system programmed in Matlab Simulink. Each C-drive is actuated by a pair of identical servomotors equipped with incremental position encoders. A number of control schemes are tested for the C-drives, including model-based controllers. As the dynamic model of the PMC is not yet available, only feedback controllers may be employed for the fully-assembled robot. To prevent damage and injury, several types of safety switches are integrated into the control system. All of the electronic hardware, with the exception of the safety switches and electromagnetic gripper[1], is reused from the McGill SMG project [13].

### 4.1.2 Computer Hardware Setup

Two computers are employed to program and run the prototype, as described below.

**Master Computer**

The control system is programmed in Matlab Simulink on the Master Computer, which runs Windows 2000 NT. Using RT-LAB version 8.1.7, the portion of the

[1] The description of these is omitted for concision.

Simulink model that must run in real-time—comprising the low level operations of the control system—is compiled as C code and loaded onto the Target Computer. The portion of the model running on the Master Computer then serves as the graphical user interface to control the prototype.

**Target Computer**

The Target Computer, running the QNX operating system, performs the control system logic and computations in real time. It interacts with the control hardware through a digital/analog I/O board, which is connected through a PCI bus. Data are exchanged with the Master Computer through a local area network.

**Servomotor Control Hardware**

The four servomotors and their control circuitry are reused from the McGill SMG. The specifications of the motors, and of the amplifiers that supply them, are found in a technical report [35].

## 4.2 C-drive Dynamics

## 4.3 Derivation of the State-space Model

The standard linear state-space representation applies to the dynamics of the C-drive:

$$\dot{\mathbf{x}} = \mathbf{A}\mathbf{x} + \mathbf{B}\mathbf{u} \tag{4.1a}$$

$$\mathbf{y} = \mathbf{C}\mathbf{x}, \qquad \mathbf{y} \equiv \boldsymbol{\psi} \tag{4.1b}$$

where $\mathbf{x}$ is the state vector, $\mathbf{u}$ the input vector, $\mathbf{y}$ the output vector, $\mathbf{A}$ the system matrix, $\mathbf{B}$ the input matrix and $\mathbf{C}$ the output matrix. The vector of Coulomb

friction $\boldsymbol{\phi}_c$ appearing in eq.(2.5) is not included here because its effect is nonlinear and nonsmooth. Non-linear models should be considered in future work.

State variables that fully describe the system are selected so as to relate to collar displacements and rates. Equations (2.1a & b) provide the required kinematic relationships. Equation (2.5) becomes

$$\mathbf{M}\mathbf{J}^{-1}\ddot{\mathbf{w}} + \mathbf{D}\mathbf{J}^{-1}\dot{\mathbf{w}} = \boldsymbol{\tau} \tag{4.2}$$

Upon premultiplication by the Jacobian $\mathbf{J}$, the foregoing *generalized coordinate model* becomes *regular*, with a symmetric, positive-definite leading coefficient, i.e.,

$$\underbrace{\mathbf{J}\mathbf{M}\mathbf{J}^{-1}}_{\mathbf{E}}\ddot{\mathbf{w}} + \underbrace{\mathbf{J}\mathbf{D}\mathbf{J}^{-1}}_{\mathbf{G}}\dot{\mathbf{w}} = \mathbf{J}\boldsymbol{\tau} \tag{4.3a}$$

$$\mathbf{E} \equiv \begin{bmatrix} e_1 & 0 \\ 0 & e_2 \end{bmatrix}, \quad \mathbf{G} \equiv \begin{bmatrix} g_1 & 0 \\ 0 & g_2 \end{bmatrix} \tag{4.3b}$$

Matrices $\mathbf{E}$ and $\mathbf{G}$ are thus *similarity transformations* [36] of $\mathbf{M}$ and $\mathbf{D}$, respectively. Notably, $\mathbf{E}$ and $\mathbf{G}$ are diagonal, their diagonal entries $e_i$ and $g_i$, $i = 1, 2$ being the eigenvalues of $\mathbf{M}$ and $\mathbf{D}$, respectively. This special case arises because the columns of $\mathbf{J}^{-1}$ are proportional to the eigenvectors of both $\mathbf{M}$ and $\mathbf{D}$. The diagonal structure of $\mathbf{E}$ and $\mathbf{G}$ reveals that the dynamics of the C-drive is decoupled from the collar coordinates. This is to be expected of an ideal cylindrical joint.

From the properties of similarity transformations, since $\mathbf{M}$ is positive-definite, so is $\mathbf{E}$, and thus $\sqrt{\mathbf{E}}$ is real and diagonal, its diagonal entries being the positive square roots of the eigenvalues of $\mathbf{E}$ [36]. Substitutions are now introduced for purposes of

model simplification:

$$\mathbf{H} \equiv \sqrt{\mathbf{E}^{-1}}\mathbf{G}\sqrt{\mathbf{E}^{-1}}, \quad \boldsymbol{\sigma} \equiv \sqrt{\mathbf{E}}\mathbf{w}, \quad \mathbf{u} \equiv \sqrt{\mathbf{E}^{-1}}\mathbf{J}\boldsymbol{\tau} \tag{4.4}$$

where

$$\sqrt{\mathbf{E}} \equiv \begin{bmatrix} \sqrt{e_1} & 0 \\ 0 & \sqrt{e_2} \end{bmatrix}, \quad \mathbf{H} \equiv \begin{bmatrix} g_1/e_1 & 0 \\ 0 & g_2/e_2 \end{bmatrix} \equiv \begin{bmatrix} h_1 & 0 \\ 0 & h_2 \end{bmatrix} \tag{4.5}$$

Equation (4.3a) is thus transformed to *monic*[2] form:

$$\ddot{\boldsymbol{\sigma}} + \mathbf{H}\dot{\boldsymbol{\sigma}} = \mathbf{u} \tag{4.6}$$

**Two-dimensional System**

An additional transformation is required to represent the system in state-space form, with a state vector $\mathbf{x}$ defined as[3]

$$\mathbf{x} \equiv \dot{\boldsymbol{\sigma}} \tag{4.7}$$

Plugging the foregoing equation into eq.(4.8) leads to a system of first-order ODE:

$$\dot{\mathbf{x}} + \mathbf{H}\mathbf{x} = \mathbf{u} \quad \Rightarrow \quad \dot{\mathbf{x}} = -\mathbf{H}\mathbf{x} + \mathbf{u} \tag{4.8}$$

[2] By analogy with polynomials, a vector $n$-order differential equation is monic if the coefficient of its highest-order term is the identity matrix.

[3] Here $\mathbf{x}$ has units of $\mathrm{m^2 kg^{1/2} s^{-1}}$

The *state-space system* is subsequently derived from eqs.(4.7) and (4.8) in the standard form of eqs.(4.1a & b), with

$$\mathbf{A} \equiv -\mathbf{H}, \quad \mathbf{B} \equiv \mathbf{1}, \quad \mathbf{C} \equiv \mathbf{J}^{-1}\sqrt{\mathbf{E}^{-1}} \tag{4.9}$$

where $\mathbf{1}$ is the $2 \times 2$ identity matrix, and vectors $\mathbf{y} \equiv \boldsymbol{\psi}$ and $\boldsymbol{\sigma}$ are obtained from the time-integration of $\dot{\boldsymbol{\psi}}$ and $\mathbf{x}$, respectively, on post-processing.

**Four-dimensional System**

A state-space system with a dimensionally homogeneous four-dimensional state vector $\mathbf{x}$ is now introduced[4]:

$$\mathbf{x} \equiv \begin{bmatrix} \boldsymbol{\sigma} \\ \\ \boldsymbol{\varsigma} \end{bmatrix}, \quad \boldsymbol{\varsigma} \equiv \mathbf{H}^{-1}\dot{\boldsymbol{\sigma}} \tag{4.10}$$

with the state-space system thus taking the standard form (4.1a & b), with

$$\mathbf{A} \equiv \begin{bmatrix} \mathbf{O} & \mathbf{H} \\ \\ \mathbf{O} & -\mathbf{H} \end{bmatrix}, \ \mathbf{B} \equiv \begin{bmatrix} \mathbf{O} \\ \\ \mathbf{H}^{-1} \end{bmatrix}, \ \mathbf{C} \equiv \begin{bmatrix} \mathbf{Y} & \mathbf{O} \end{bmatrix}, \ \mathbf{Y} \equiv \mathbf{J}^{-1}\sqrt{\mathbf{E}^{-1}}, \ \mathbf{y} \equiv \boldsymbol{\psi} \tag{4.11}$$

where $\mathbf{O}$ is the $2 \times 2$ zero matrix. This system eliminates the need for post-processing but is more complex than the previous representation. The matrix $\mathbf{H}^{-1}$ is readily available, as $\mathbf{H}$ is diagonal, besides being of $2 \times 2$.

[4] Here $\mathbf{x}$ has units of $\mathrm{m}^2\mathrm{kg}^{1/2}$

## 4.4 Controllability and Observability of the C-drive

### 4.4.1 Two-dimensional System

The state-space representations of the dynamics of the C-drive are linear time-invariant systems. For the system from eq.(4.9), the controllability matrix [37] is thus derived as

$$\mathbf{\Gamma}_2 \equiv [\mathbf{B} \quad \mathbf{AB}] = [\mathbf{1} \quad -\mathbf{H}] \tag{4.12}$$

Since the two $2 \times 2$ blocks of $\mathbf{\Gamma}_2$ are of full rank, this $2 \times 4$ controllability matrix has full rank. The C-drive is thus completely controllable.

The $4 \times 2$ observability matrix is derived in turn as

$$\mathbf{\Omega}_2 \equiv \begin{bmatrix} \mathbf{Y} \\ \\ \mathbf{YA} \end{bmatrix} = \begin{bmatrix} \mathbf{J}^{-1}\sqrt{\mathbf{E}}^{-1} \\ \\ -\mathbf{J}^{-1}\sqrt{\mathbf{E}}^{-1}\mathbf{H} \end{bmatrix} \tag{4.13}$$

where $\mathbf{J}^{-1}$ and $\sqrt{\mathbf{E}}^{-1}$ are available, as $\mathbf{J}$ and $\sqrt{\mathbf{E}}$ are invertible, $\mathbf{\Omega}_2$ thus having full rank. This system is thus completely observable. It is, however, not useful to construct an observer for this system. The state vector $\mathbf{x}$ is obtained algebraically from the output vector $\dot{\boldsymbol{\psi}}$ using eqs.(2.1a), (4.4) and (4.7):

$$\mathbf{x} = \sqrt{\mathbf{E}}\mathbf{J}\dot{\boldsymbol{\psi}} \tag{4.14}$$

As $\dot{\boldsymbol{\psi}}$ cannot be measured by the C-drive prototype encoders, which provide $\boldsymbol{\psi}$, $\mathbf{x}$ cannot be estimated by an observer using this system.

### 4.4.2 Four-dimensional System

Estimating $\mathbf{x} \equiv \dot{\boldsymbol{\sigma}}$ by means of an observer is desirable in order to avoid numerical differentiations, which introduce noise. The four-dimensional system (4.10–4.11)

has $\boldsymbol{\psi}$ as its output, which is directly measured. The controllability and observability of the system are now assessed, and an observer is designed to estimate $\mathbf{x}$.

**Controllability**

The $4 \times 8$ controllability matrix is derived as

$$\boldsymbol{\Gamma}_4 \equiv \begin{bmatrix} \mathbf{B} & \mathbf{AB} & \mathbf{A}^2\mathbf{B} & \mathbf{A}^3\mathbf{B} \end{bmatrix} \tag{4.15}$$

Plugging in matrices $\mathbf{A}$ and $\mathbf{B}$ from eq.(4.11) leads to

$$\boldsymbol{\Gamma}_4 = \left[\begin{array}{cc|cc} \mathbf{O} & \mathbf{1} & -\mathbf{H} & \mathbf{H}^2 \\ \mathbf{H}^{-1} & -\mathbf{1} & \mathbf{H} & -\mathbf{H}^2 \end{array}\right] \tag{4.16}$$

$$\underbrace{\qquad\qquad}_{\boldsymbol{\Gamma}_{4a}} \qquad \underbrace{\qquad\qquad}_{\boldsymbol{\Gamma}_{4b}}$$

where $\boldsymbol{\Gamma}_{4a}$ is

$$\boldsymbol{\Gamma}_{4a} \equiv \left[\begin{array}{cc|cc} 0 & 0 & 1 & 0 \\ 0 & 0 & 0 & 1 \\ \hline 1/h_1 & 0 & -1 & 0 \\ 0 & 1/h_2 & 0 & -1 \end{array}\right] \tag{4.17}$$

$$\underbrace{\qquad\qquad}_{\boldsymbol{\Gamma}_{4a(i)}} \qquad \underbrace{\qquad\qquad}_{\boldsymbol{\Gamma}_{4a(ii)}}$$

The columns of $\boldsymbol{\Gamma}_{4a(i)}$ on the one hand and of $\boldsymbol{\Gamma}_{4a(ii)}$ on the other are clearly linearly independent for any finite values of $h_1$ and $h_2$, that is, the diagonal entries of $\mathbf{H}$. Upon inspection of the upper $2 \times 2$ blocks of the foregoing matrices, the $2 \times 2$ zero and identity matrices, it is apparent that the columns of $\boldsymbol{\Gamma}_{4a(i)}$ and $\boldsymbol{\Gamma}_{4a(ii)}$ are linearly independent. $\boldsymbol{\Gamma}_{4a}$ is therefore nonsingular, that is, of rank four, and the controllability matrix $\boldsymbol{\Gamma}_4$ has full rank. This system is thus completely controllable.

**Observability**

The next step is to determine whether the system is observable. The observability matrix is defined as

$$\mathbf{\Omega}_4 \equiv \begin{bmatrix} \mathbf{C} \\ \mathbf{CA} \\ \mathbf{CA}^2 \\ \mathbf{CA}^3 \end{bmatrix} = \left[\begin{array}{cc} \mathbf{Y} & \mathbf{O} \\ \mathbf{O} & -\mathbf{YH} \\ \hline \mathbf{O} & -\mathbf{YH}^2 \\ \mathbf{O} & -\mathbf{YH}^3 \end{array}\right] \begin{matrix} \Big\} \mathbf{\Omega}_{4a} \\ \Big\} \mathbf{\Omega}_{4b} \end{matrix} \tag{4.18}$$

From eq.(4.9), it is apparent that $\mathbf{Y}$ is nonsingular for finite $\nu_1$ and $\nu_2$, while matrix $\mathbf{YH}$, given by

$$\mathbf{YH} \equiv \frac{2\pi}{p} \begin{bmatrix} g_1 e_1^{-2/3} & g_2 e_2^{-2/3} \\ -g_1 e_1^{-2/3} & g_2 e_2^{-2/3} \end{bmatrix} \tag{4.19}$$

is nonsingular. Matrices $\mathbf{Y}$ and $-\mathbf{YH}$ are the diagonal blocks of the block-diagonal submatrix $\mathbf{\Omega}_{4a}$, which is therefore nonsingular; hence, $\mathbf{\Omega}_4$ is of full rank. As a consequence, the system at hand is completely observable.

**Minimum-Order State Observer**

The state vector $\mathbf{x}$ can be estimated by a Luenberger full-order state observer as the system is linear and time-invariant [38]. For convenience, the definition of $\mathbf{x}$

is recalled:

$$\mathbf{x} \equiv \begin{bmatrix} \boldsymbol{\sigma} \\ \\ \boldsymbol{\varsigma} \end{bmatrix}, \quad \boldsymbol{\varsigma} \equiv \mathbf{H}^{-1}\dot{\boldsymbol{\sigma}} \tag{4.20a}$$

$$\dot{\boldsymbol{\sigma}} \equiv \sqrt{\mathbf{E}}\dot{\mathbf{w}} = \sqrt{\mathbf{E}}\mathbf{J}\dot{\boldsymbol{\psi}}, \quad \boldsymbol{\sigma} \equiv \sqrt{\mathbf{E}}\mathbf{w} = \sqrt{\mathbf{E}}\mathbf{J}\boldsymbol{\psi} \tag{4.20b}$$

where $\mathbf{w}$ and $\boldsymbol{\psi}$ are the vectors of collar and motor displacements, respectively, and the generalized coordinate model of the system is

$$\mathbf{E}\ddot{\mathbf{w}} + \mathbf{G}\dot{\mathbf{w}} = \mathbf{J}\boldsymbol{\tau} \tag{4.20c}$$

from which

$$\mathbf{H} \equiv \sqrt{\mathbf{E}}^{-1}\mathbf{G}\sqrt{\mathbf{E}}^{-1} \tag{4.20d}$$

States $\boldsymbol{\sigma}$ are computed algebraically from the motor-encoder readouts $\boldsymbol{\psi}$ via eq.(4.20b). A full-order state observer—producing an estimate of $\mathbf{x}$—estimates $\boldsymbol{\sigma}$ with lower accuracy than the foregoing scheme. A minimum-order state observer that only estimates the second (unmeasured) component of $\mathbf{x}$, namely $\boldsymbol{\varsigma}$, is therefore required [39]. This type of observer has the further advantage that the desired state estimate generally converges more quickly than with the corresponding full-order state observer [37].

The state and input matrices, $\mathbf{A}$ and $\mathbf{B}$ are recalled from eq.(4.11) for convenience:

$$\mathbf{A} \equiv \begin{bmatrix} \mathbf{A}_{11} & \mathbf{A}_{12} \\ \\ \mathbf{A}_{21} & \mathbf{A}_{22} \end{bmatrix} \equiv \begin{bmatrix} \mathbf{O} & \mathbf{H} \\ \\ \mathbf{O} & -\mathbf{H} \end{bmatrix}, \quad \mathbf{B} \equiv \begin{bmatrix} \mathbf{B}_1 \\ \\ \mathbf{B}_2 \end{bmatrix} \equiv \begin{bmatrix} \mathbf{O} \\ \\ \mathbf{H}^{-1} \end{bmatrix} \tag{4.21}$$

The minimum-order observer is defined by the system [39]:

$$\boldsymbol{\kappa} \equiv \boldsymbol{\varsigma} - \mathbf{L}\boldsymbol{\sigma} \quad \Leftrightarrow \quad \widetilde{\boldsymbol{\kappa}} \equiv \widetilde{\boldsymbol{\varsigma}} - \mathbf{L}\boldsymbol{\sigma} \tag{4.22a}$$

$$\dot{\widetilde{\boldsymbol{\kappa}}} = \mathbf{U}\widetilde{\boldsymbol{\kappa}} + \mathbf{V}\boldsymbol{\sigma} + \mathbf{Z}\mathbf{u} \tag{4.22b}$$

where $(\widetilde{\cdot})$ denotes an estimate of the variable $(\cdot)$, $\dot{\widetilde{\boldsymbol{\kappa}}}$ being the derivative of $\widetilde{\boldsymbol{\kappa}}$, and the $2 \times 2$ matrix coefficients of eq.(4.22b) are defined as

$$\mathbf{U} \equiv \mathbf{A}_{22} - \mathbf{L}\mathbf{A}_{12}, \quad \mathbf{V} \equiv \mathbf{U}\mathbf{L} + \mathbf{A}_{21} - \mathbf{L}\mathbf{A}_{11}, \quad \mathbf{Z} \equiv \mathbf{B}_2 - \mathbf{L}\mathbf{B}_1 \tag{4.22c}$$

Hence

$$\mathbf{U} \equiv -(\mathbf{1} + \mathbf{L})\,\mathbf{H}, \quad \mathbf{V} \equiv \mathbf{U}\mathbf{L} = -(\mathbf{1} + \mathbf{L})\,\mathbf{H}\mathbf{L}, \quad \mathbf{Z} \equiv \mathbf{H}^{-1} \tag{4.22d}$$

The state vector estimate is then obtained from the relation

$$\widetilde{\mathbf{x}} = \boldsymbol{\Phi}\widetilde{\boldsymbol{\kappa}} + \boldsymbol{\Lambda}\boldsymbol{\sigma}, \quad \widetilde{\mathbf{x}} \equiv \begin{bmatrix} \boldsymbol{\sigma} \\ \\ \widetilde{\boldsymbol{\varsigma}} \end{bmatrix} \tag{4.22e}$$

with

$$\boldsymbol{\Phi} \equiv \begin{bmatrix} \mathbf{O} \\ \\ \mathbf{1} \end{bmatrix}, \quad \boldsymbol{\Lambda} \equiv \begin{bmatrix} \mathbf{1} \\ \\ \mathbf{L} \end{bmatrix} \tag{4.22f}$$

where $\mathbf{L}$ is the $2 \times 2$ matrix of observer feedback gains. The observer error equation is then defined as

$$\dot{\boldsymbol{\epsilon}} = \mathbf{U}\boldsymbol{\epsilon} \tag{4.23a}$$

where

$$\boldsymbol{\epsilon} \equiv \boldsymbol{\varsigma} - \widetilde{\boldsymbol{\varsigma}} = \boldsymbol{\kappa} - \widetilde{\boldsymbol{\kappa}} \tag{4.23b}$$

Matrix $\mathbf{L}$ is computed upon selection of the poles of the observer. The system matrices of the C-drive minimum-order state observer are $\mathbf{A}_{12} \equiv \mathbf{H}$, $\mathbf{A}_{22} \equiv -\mathbf{H}$ and

$\mathbf{B}_2 \equiv \mathbf{H}^{-1}$ from eq.(4.21). Recalling the definition of $\mathbf{H}$ in eq.(4.5), this matrix is constructed from the generalized inertia matrix $\mathbf{M}$ and damping matrix $\mathbf{D}$ of the C-drive. As the two forgoing matrices are only known approximately, and in particular $\mathbf{D}$ is affected by environmental factors and wear, significant perturbations in $\mathbf{H}$ are expected. A robust pole-placement algorithm is performed numerically in Matlab using the `place()` function [39, 40], with the arguments

$$\mathbf{L} = \texttt{place}\left(\mathbf{A}_{22}^T,\, \mathbf{A}_{12}^T,\, [\lambda_1 \quad \lambda_2]\right) \tag{4.24}$$

where the transpose superscript may be omitted because $\mathbf{A}_{12}$ and $\mathbf{A}_{22}$ are both symmetric, and $\lambda_1$ and $\lambda_2$ are the observer poles. The poles may be selected arbitrarily as the minimum-order system is completely observable, the proof of which is left out for conciseness. The closed-loop poles are selected such that their real parts are negative—in order for the observer to be asymptotically stable—and that they form a complex-conjugate pair—to reduce the effects of nonlinearities such as backlash:

$$\mathrm{Re}\left(\lambda_1\right),\, \mathrm{Re}\left(\lambda_2\right) < 0, \qquad \lambda_1 = \bar{\lambda}_2 \tag{4.25}$$

### 4.5 Time Response of the C-drive

The time response of the C-drive can be obtained symbolically, to be used in simulation. The matrix $\mathrm{e}^{\mathbf{A}t}$ is readily computed:

$$\mathrm{e}^{\mathbf{A}t} \equiv \begin{bmatrix} \mathrm{e}^{-h_1 \mathrm{t}} & 0 \\ 0 & \mathrm{e}^{-h_2 \mathrm{t}} \end{bmatrix} \tag{4.26}$$

The time response of the system takes the form [37]:

$$\mathbf{x}(t) = \mathrm{e}^{\mathbf{A}t}\mathbf{x}_0 + \int_0^t \mathrm{e}^{\mathbf{A}(t-\tau)}\mathbf{u}(\tau)\,d\tau \tag{4.27}$$

for a given initial state $\mathbf{x}_0$. Recalling eqs.(4.4) and (4.7), the velocity $\dot{\mathbf{w}}$ of the collar is computed from

$$\dot{\mathbf{w}} = \sqrt{\mathbf{E}}^{-1}\mathbf{x} \tag{4.28}$$

while the joint rates $\dot{\boldsymbol{\psi}}$ are obtained from eq.(2.4). Meanwhile, the joint and collar displacements are obtained from the definite time integral of $\mathbf{x}(t)$. First, vector $\boldsymbol{\sigma}(t)$ is computed:

$$\boldsymbol{\sigma}(t) = \int_0^t \mathbf{x}(\varphi)\,d\varphi + \boldsymbol{\sigma}_0 \tag{4.29a}$$

$$= \underbrace{\int_0^t \mathrm{e}^{\mathbf{A}\varphi}\mathbf{x}_0\,d\varphi}_{\mathbf{z}_1(t)} + \underbrace{\int_0^t\int_0^\varphi \mathrm{e}^{\mathbf{A}(\varphi-\tau)}\mathbf{u}(\tau)\,d\tau\,d\varphi}_{\mathbf{z}_2(t)} + \boldsymbol{\sigma}_0 \tag{4.29b}$$

where $\boldsymbol{\sigma}_0$ is the initial value of $\boldsymbol{\sigma}$, and hence,

$$\mathbf{z}_1(t) \equiv \begin{bmatrix} \left(1-\mathrm{e}^{-h_1\mathrm{t}}\right)h_1^{-1} & 0 \\ 0 & \left(1-\mathrm{e}^{-h_2\mathrm{t}}\right)h_2^{-1} \end{bmatrix} \underbrace{\begin{bmatrix} \sqrt{e_1}\nu_0 \\ \sqrt{e_2}\zeta_0 \end{bmatrix}}_{\mathbf{x}_0} \tag{4.29c}$$

with $\nu_0$ and $\zeta_0$ being the initial values of the collar rates $\dot{u}$ and $\dot{v}$, and $e_i$, $i = 1, 2$, the diagonal entries of $\mathbf{E}$. A closed-form expression for $\mathbf{z}_2$ may be available, depending on the nature of vector $\mathbf{u}(\tau)$. Finally, the displacement vector of the collar, namely $\mathbf{w}$, is obtained from the expression

$$\mathbf{w} = \sqrt{\mathbf{E}}^{-1}\boldsymbol{\sigma} \tag{4.30}$$

## 4.6 C-drive Controllers

### 4.6.1 Ideal PID Controller

The PID controller is the most common class of feedback controller used in industry [41]. It is a closed-loop controller that minimizes the Euclidean norm of the *error*, defined as

$$\mathbf{e}(t) \equiv \boldsymbol{\psi}_d(t) - \mathbf{y}(t) \tag{4.31}$$

where $\boldsymbol{\psi}_d$ is the desired reference signal, and $\mathbf{y}$ is the process variable, which is being controlled. The PID controller may be expressed in its *ideal form* as

$$\boldsymbol{\tau}(t) = \mathbf{K}_P\mathbf{e}(t) + \mathbf{K}_I \int \mathbf{e}(t)\, dt + \mathbf{K}_D\dot{\mathbf{e}}(t) \tag{4.32}$$

where $\boldsymbol{\tau}$ is the manipulated variable output by the controller, while $\mathbf{K}_P$, $\mathbf{K}_I$ and $\mathbf{K}_D$ are the proportional, integral and derivative gain matrices of the controller, respectively. For the C-drive, $\boldsymbol{\tau}$ is the vector of motor torques and $\mathbf{y}$ is the vector of motor displacements as measured by shaft encoders.

### 4.6.2 PD Controller Implementation

#### Cascade Controller

The PID controller is the outer loop of a cascade controller driving the motors. Its output is more accurately denoted $\boldsymbol{\tau}_o$, the output torque[5]. The PI controller implemented in the servomotor amplifiers tracks $\boldsymbol{\tau}_o$ such that the motors output the torque $\boldsymbol{\tau}$. A simplified schematic of the full controller is shown in Fig. 4–1.

[5] The motors are used in torque control mode.

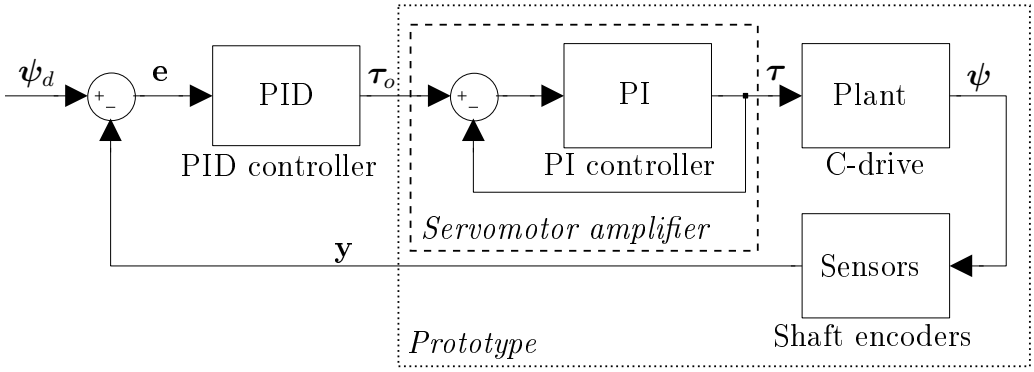


Figure 4–1: Block-diagram of PID controller, with PI torque control loop

The inner loop is tuned to have a very short settling time[6]. It is therefore assumed that $\boldsymbol{\tau}_o$ and $\boldsymbol{\tau}$ are equal, and the loop is safely neglected in the rest of the analysis of the control system. All servo amplifier parameters are reported in Appendix A.

**Controller Selection**

It is often not necessary to use both the differential and integral components of PID controllers. The most common type of controller used in industry is the PI controller, for which $\mathbf{K}_d$ is absent [42]. This controller avoids the often difficult task of obtaining a low noise derivative of the error signal. This is the first type of controller to be implemented for the C-drives, as reported in [26]. When high-damping flexible shaft couplings were substituted for high torsional-rigidity couplings to improve perfomance, the PI controller could not be made stable at the high PI gain

[6] Yaskawa technical support suggested a loop time of approximately half of the controller sample time, namely 1 ms.

values required for high speed operation. The controller was therefore substituted with a PD controller, that is, with $\mathbf{K}_I$ absent.

### 4.6.3 Model-based Controller

As the dynamic model of the C-drive is available, model-based controllers can be developed to improve upon the performance of the PD controller. The most common type of model-based controller is the feedforward controller, which uses the inverse dynamic model to predict the required actuator effort based on the desired motor displacements, speeds and accelerations. The predicted *corrective torques* are then added to the output $\ddot{\boldsymbol{\psi}}_o$ of the PD-controller [43]. Therefore, the PD controller is independent of—and perturbed by—the corrective torques. This issue is addressed by the *computed-torque control* (CTC) method, introduced by Markiewicz [44] and discussed in detail by Khosla and Kanade [45]. Here the PD control portion generates *corrective accelerations*, which, added to the desired accelerations, are input into the inverse dynamics.

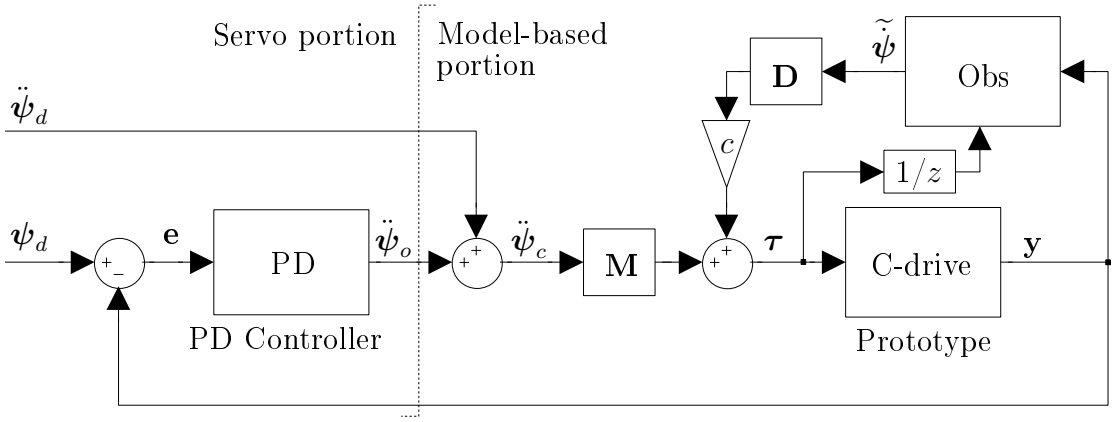


Figure 4–2: Block diagram of computed-torque controller

In CTC, the corrective acceleration $\ddot{\boldsymbol{\psi}}_c$ is computed from

$$\ddot{\boldsymbol{\psi}}_c = \ddot{\boldsymbol{\psi}}_d + \underbrace{\mathbf{K}_P\mathbf{e} + \mathbf{K}_D\dot{\mathbf{e}}}_{\ddot{\boldsymbol{\psi}}_o} \tag{4.33}$$

where $\ddot{\boldsymbol{\psi}}_d$ is the vector of desired motor accelerations. Equation (2.5) readily yields the inverse dynamics, that is, the expression for motor torque $\boldsymbol{\tau}$. Substituting motor accelerations $\ddot{\boldsymbol{\psi}}$ with $\ddot{\boldsymbol{\psi}}_c$ leads to

$$\boldsymbol{\tau} = \mathbf{M}\ddot{\boldsymbol{\psi}}_c + \mathbf{D}\dot{\boldsymbol{\psi}} \tag{4.34}$$

The value of $\dot{\boldsymbol{\psi}}$ is estimated by the observer described in Section 4.4.2, yielding $\widetilde{\dot{\boldsymbol{\psi}}}$. The friction compensation torque is therefore $\mathbf{D}\widetilde{\dot{\boldsymbol{\psi}}}$. The viscous friction model is a significant simplification of the true frictional dynamics of the C-drive, neglecting many effects such as stiction and Coulomb friction. In order to avoid perturbing the computed torque with an inaccurate friction compensation torque, the latter is multiplied by a scalar *friction compensation gain*, denoted $c$ and tuned experimentally, thereby leading to the complete formulation of the computed torque:

$$\boldsymbol{\tau} = \mathbf{M}\ddot{\boldsymbol{\psi}}_c + c\mathbf{D}\widetilde{\dot{\boldsymbol{\psi}}} \tag{4.35}$$

The block diagram of this computed-torque controller is represented in Fig. 4–2. The block marked "$1/z$" is a unit delay, that is, it delays the torque signal to the observer by one time step, namely 1 ms in our case. The delay is required to avoid an algebraic loop in the computation of $\boldsymbol{\tau}$.

### 4.6.4 Task-space Controller

The PD and CT controllers are said to be *joint-space* controllers, as the error vector $\mathbf{e}$ is computed from joint variables, namely the motor displacements. It is often advantageous to use task-space (TS) control, also referred to as Cartesian [46] or contouring [47] control, in which the error is computed in terms of the task performed by the mechanism. In the case of the C-drive, the task variables are the collar coordinates $\mathbf{w}$. The TS error $\boldsymbol{\varepsilon}$ is defined as

$$\boldsymbol{\varepsilon} \equiv \mathbf{w}_d - \mathbf{w} = \mathbf{J}\mathbf{e} \tag{4.36}$$

where $\mathbf{w}_d$ is the vector of desired collar coordinates. Moreover, $\boldsymbol{\varepsilon}$ is computed from motor coordinates by means of the right-hand side of the foregoing equation.

In C-drive tests with the joint-space PD controller, it was found that higher gains could be used for the pure-rotation motion program than for its translation counterpart without incurring instability, thus leading to improved performance in the rotation tests. TS controllers have independent gains for rotation and translation of the collar, which are tuned as required for the task.

**TS PD controller**

A TS PD control scheme is defined as

$$\boldsymbol{\tau}_o = \mathbf{J}^{-1}\mathbf{K}_P \underbrace{\mathbf{J}\mathbf{e}}_{\boldsymbol{\varepsilon}} + \mathbf{J}^{-1}\mathbf{K}_D \underbrace{\mathbf{J}\dot{\mathbf{e}}}_{\dot{\boldsymbol{\varepsilon}}} \tag{4.37a}$$

where the PD gain matrices are

$$\mathbf{K}_P \equiv \begin{bmatrix} k_P^t & 0 \\ 0 & k_P^r \end{bmatrix}, \quad \mathbf{K}_D \equiv \begin{bmatrix} k_D^t & 0 \\ 0 & k_D^r \end{bmatrix} \tag{4.37b}$$

and the $t$ and $r$ supercripts refer to collar translation and rotation gains, respectively. When the translation and rotation gains are equal, namely

$$k_I^t = k_I^r,\ I = P,\ D \tag{4.38}$$

then eq.(4.37a) becomes identical to the joint-space PD scheme from eq.(4.32). Therefore, the TS PD controller can be used as a joint-space controller.

**Model-based TS Controller**

The TS control counterpart of the CT controller is the *resolved-acceleration controller* [48]. It operates like the CT controller, except that the output acceleration $\ddot{\boldsymbol{\psi}}_o$ from the servo portion is now defined as $\boldsymbol{\tau}_o$ from eq.(4.37a).

In experiments, the resolved-acceleration controller became unstable when $k_P^t \neq k_P^r$, that is, when it was different from a joint-space CT controller. The cause of this phenomenon is not known, but further work on the controller was not pursued. In future sections, the name "TS controller" *refers only to the PD TS controller.*

# CHAPTER 5
# Experimental Results

## 5.1 C-drive Results

### 5.1.1 Controller Tuning

#### PD Controller Tuning

For a PD controller in the ideal form, three parameters must be tuned, namely gains $\mathbf{K}_P$, $\mathbf{K}_D$, and the derivative filter coefficient $N$.

**Derivative Filter.** There are many methods for obtaining the derivative of the error signal, such as the continuous time methods reported by Visioli [41] and the discrete-time methods reported by Åström and Wittenmark [49]. The simplest and most common continuous-time method is used to keep the complexity of the controller as low as possible. The transfer function of the filter is defined as

$$F(s) \equiv \frac{Ns}{N+s} \tag{5.1}$$

where $s$ is the Laplace-transform variable, and the pole of the filter is located at $-N$. This filter is readily designed in Simulink and implemented on the Target Computer.

**PD Gain Tuning.** The high-gain PD controller is tuned experimentally based on the method suggested by Ellis [42]. $\mathbf{K}_P$ and $\mathbf{K}_D$ are diagonal $2 \times 2$ matrices,

whose diagonal terms are identical[1] and denoted $k_P$ and $k_D$ respectively. Initial low proportional and derivative gains are selected arbitrarily. Gain $k_P$ is then increased until just below the limit of stability of the controller; $k_D$ is then increased until the controller is stable. This process is repeated until the highest $k_P$ is selected such that the controller remains stable in testing. The parameters are reported in Table 5–1.

This simple experimental method cannot guarantee optimal gains, but allows for the control system to be tuned sufficiently well to demonstrate the performance of the proof-of-concept C-drive.

### 5.1.2 Computed-torque Controller

The CTC has two portions, the servo portion that tracks motor displacement errors, and the model-based portion that compensates for the C-drive dynamics.

**Servo Portion.** The servo portion functions identically to the PD controller, and is tuned using the same method. The parameters are reported in Table 5–1.

**Dynamics Compensation.** The value of the generalized inertia matrix $\mathbf{M}$ is computed in CAD software:

$$\mathbf{M} = \begin{bmatrix} 2.6312 & 1.8797 \\ 1.8797 & 2.6312 \end{bmatrix} \text{ gm}^2 \tag{5.2}$$

The values of the damping matrix $\mathbf{D}$ were obtained experimentally using tests similar to those proposed by Virgala and Kelemen [50], and are reported by Harada et al. [26].

[1] It was found experimentally that the same gains may be used for each motor, thus simplifying tuning. However, the control software does allow for separate gains to be set.

Table 5–1: Controller tuning parameters

| **Controller:** | **PD** | **CTC** | **TS** |
|---|---|---|---|
| $k_P$ | 45 Nm/rad | 35000 $s^{-2}$ | $trans: 45, \quad rot: 112.5$ Nm/rad |
| $k_D$ | .1 Nms/rad | 55 $s^{-1}$ | $trans: 0.1, \quad rot: 0.25$ Nms/rad |
| $N$ | 600 rad/s | 600 rad/s | 600 rad/s |
| $\lambda_i$ | – | $-600$ rad/s | – |
| $c$ | – | 0.4 | – |

In simulation, a 5% error is introduced to the estimates of **M** and **D** in the model-based portion of the controller, to account for uncertainty in their values.

The model-based portion requires tuning of both the observer and the friction compensation gain. The observer has two poles, $\lambda_i$, $i = 1, 2$, resulting in a gain matrix **L** found using the procedure from Section 4.4.2.

In experimental tests, the friction compensation gain $c$ was then varied between 0 and 1.5 in all motion programs. The value $c = 0.4$ consistently produced the lowest absolute error in motor displacements, and was retained[2].

### 5.1.3 TS Controller Tuning

The TS PD controller, referred to as the TS controller for short, is tuned using the same approach as the joint-space PD controller. The controller parameters are listed in Table 5–1.

[2] In simulations, the value $c \approx 1$ produced the best results, as expected.

Table 5–2: Scaling coefficients for each motion program

| **Joint Rates** | **Motion** | $\boldsymbol{\alpha_I}$ **(rad)** |
|---|---|---|
| $\dot{\psi_L} = -\dot{\psi_R}$ | pure translation (200 mm) | $\alpha_L = -20\pi/3, \quad \alpha_R = 20\pi/3$ |
| $\dot{\psi_L} = \dot{\psi_R}$ | pure rotation ($\pi$ rad) | $\alpha_L = \alpha_R = \pi$ |
| $\lvert\dot{\psi_L}\rvert \neq \lvert\dot{\psi_R}\rvert$ | helical motion (100 mm and $\pi/2$ rad) | $\alpha_L = -17\pi/6, \quad \alpha_R = 23\pi/6$ |

### 5.1.4 Benchmark Tests

#### Test Parameters

The analysis of C-drive performance is carried out on three benchmark motion programs, demonstrating pure translation, pure rotation and combined translation and rotation—helical motion. As reported earlier [26], a smooth polynomial is used to define the motion programs. Zero velocity, acceleration and jerk are obtained at the endpoints of the motion through the use of a 4-5-6-7 polynomial $s(\tau)$, namely

$$s(\tau) = -20\tau^7 + 70\tau^6 - 84\tau^5 + 35\tau^4 \tag{5.3}$$

where $0 \leq s \leq 1$ and $0 \leq \tau \leq 1$, $\tau$ being nondimensional time. The prescribed motor displacements become:

$$\psi_I(t) = \begin{cases} \alpha_I s(t) & 0 \leq t \leq t_{max}/2 \\ \alpha_I s(t_{max} - t) & t_{max}/2 < t \leq t_{max} \end{cases}, \qquad I = R,\, L \tag{5.4a}$$

$$t = \tau t_{max} \tag{5.4b}$$

where $t_{max}$ is the total cycle time, and scaling coefficients $\alpha_I$ are given in Table 5–2.

### Simulation Parameters

The offline simulation and real-time control system are both programmed in Simulink using the same simulation parameters, reported in Table 5–3.

Table 5–3: Simulation Parameters

| | |
|---|---|
| Solver type: | Fixed-step |
| Step size: | 1 ms |
| Solver: | ODE4 (Runge-Kutta) |

### Test Metrics

Data are recorded at each 1 ms controller time step by the Target PC during experimental C-drive testing, namely, controller error $\mathbf{e}$ and motor torques $\boldsymbol{\tau}$. Collar displacement error $\boldsymbol{\varepsilon}$ is obtained upon transformation of the error in motor displacements by the Jacobian $\mathbf{J}$, defined in eq.(2.1b). This kinematic relation assumes that the C-drive is made of rigid bodies and that the ballscrews are perfect helical joints.

**Measurement Limitations.** Motor displacements, and thus error, is measured at $2^{13}$ bit resolution by the shaft encoders. Measurement tools were not available to calibrate the motor torque output; the control torque value is thus assumed to be accurate. In simulations, control torques are assumed to be identical to motor output torques, and motor displacements are quantized to the same resolution as the encoders.

**Metrics for Comparison.** Metrics are required to compare the torque and error performance of the three controllers:

**RMS** The well-known root mean square (RMS) analysis quantifies overall performance; values are averaged over several consecutive test cycles.

**Maximum Torque** The maximum absolute value of motor torque over each test cycle is recorded and averaged. These data are needed to avoid motor saturation.

**Error at Cycle Endpoints** For pick-and-place operations, the error at cycle endpoints must be minimal. The values are averaged over several test cycles.

**Test Results**

**2 Hz Tests.** All motion programs are tested both in simulation and experimentally. The 4-5-6-7 polynomial over a 500 ms cycle, $s(t)$, and its normalized first and second derivatives, $\dot{\bar{s}}(t)$ and $\ddot{\bar{s}}(t)$, are shown in Fig. 5–1a. The three motion programs in collar coordinates appear in Figs. 5–1b to 5–1d. The translation and rotation error curves for the helical motion program are compared in Figs. 5–1f and 5–1e, respectively. Experimental and simulation results are compared in Fig. 5–2: the PD, CT and TS controller results are shown for the rotation, translation and helical motion programs, respectively, as this subset of tests suffices to illustrate the performance of the C-drive. The torque curve of the left motor is omitted as it displays the same behaviour as the right motor.

The RMS values from experimental and simulated tests are shown in Table 5–4. $\bar{\tau}$ is the average of left and right motor torque results (in Nm), while $e_u$ and $e_\theta$ are collar translation error (in mm) and rotation error (in rad), respectively.

The RMS results are processed in two ways. Table 5–5 shows the percentage error in RMS simulation results compared to experimental data. Table 5–6 compares the performance of the three controllers by showing the percentage difference between the PD controller results and those of the CT and TS controllers.

Table 5–4: RMS results, 2 Hz tests

| Motion | RMS | PD Exp. | CT Exp. | TS Exp. | PD Sim. | CT Sim. | TS Sim. |
|---|---|---|---|---|---|---|---|
| trans. | $\bar{\tau}$ | 1.4354 | 1.3434 | 1.3148 | 1.4760 | 1.4693 | 1.4760 |
| | $e_u$ | 0.3057 | 0.3548 | 0.2751 | 0.3200 | 0.1811 | 0.3200 |
| | $e_\theta$ | 0.0037 | 0.0009 | 0.0009 | 0.0000 | 0.0000 | 0.0000 |
| rot. | $\bar{\tau}$ | 1.0997 | 1.0391 | 1.0476 | 1.2480 | 1.1471 | 1.1810 |
| | $e_u$ | 0.0037 | 0.0059 | 0.0043 | 0.0000 | 0.0000 | 0.0000 |
| | $e_\theta$ | 0.0249 | 0.0054 | 0.0092 | 0.0283 | 0.0012 | 0.0111 |
| helical | $\bar{\tau}$ | 0.8024 | 0.7861 | 0.8030 | 0.8400 | 0.8139 | 0.8256 |
| | $e_u$ | 0.1574 | 0.1730 | 0.1535 | 0.1616 | 0.0936 | 0.1631 |
| | $e_\theta$ | 0.0119 | 0.0023 | 0.0044 | 0.0141 | 0.0003 | 0.0053 |

Table 5–5: Percentage error in RMS simulation predictions, 2 Hz tests

| Motion Type | RMS % Error | PD Sim. | CT Sim. | TS Sim. |
|---|---|---|---|---|
| translational | $\bar{\tau}$ | 2.83 | 9.37 | 12.27 |
| | $e_u$ | 4.68 | −48.96 | 16.32 |
| | $e_\theta$ | – | – | – |
| rotational | $\bar{\tau}$ | 13.49 | 10.39 | 12.74 |
| | $e_u$ | – | – | – |
| | $e_\theta$ | 13.61 | −78.48 | 20.89 |
| helical | $\bar{\tau}$ | 4.69 | 3.54 | 2.82 |
| | $e_u$ | 2.64 | −45.93 | 6.27 |
| | $e_\theta$ | 18.89 | −86.16 | 19.65 |

The average error in collar displacements at cycle endpoints is shown in Table 5–7. The maximum absolute error and torque values are reported in Table 5–8, where $\tau_{max}$ denotes the larger absolute torque output of the two motors.

**1 Hz Tests.** The same motion programs were tested with a 1 Hz cycle. For conciseness, only experimental RMS data are reported, along with the percentage difference of CT and TS, as compared to PD control, in Table 5–9.

Table 5–6: Percentage difference of CT, TS vs. PD controller, 2 Hz tests

| Motion Type | RMS % Difference | CT Exp. | TS Exp. | CT Sim. | TS Sim. |
|---|---|---|---|---|---|
| translational | $\bar{\tau}$ | −6.41 | −8.40 | −0.46 | 0.00 |
| | $e_u$ | 16.07 | −10.00 | −43.41 | 0.00 |
| | $e_\theta$ | −74.92 | −75.87 | 0.00 | 0.00 |
| rotational | $\bar{\tau}$ | −5.51 | −4.74 | −8.08 | −5.37 |
| | $e_u$ | 60.94 | 18.62 | 0.00 | 0.00 |
| | $e_\theta$ | −78.24 | −62.97 | −95.88 | −60.60 |
| helical | $\bar{\tau}$ | −2.03 | 0.07 | −3.11 | −1.72 |
| | $e_u$ | 9.92 | −2.49 | −42.09 | 0.96 |
| | $e_\theta$ | −80.88 | −62.77 | −97.77 | −62.53 |

Table 5–7: Average error at cycle endpoints, 2 Hz tests

| Motion | $e_i$ | PD Exp. | CT Exp. | TS Exp. | PD Sim. | CT Sim. | TS Sim. |
|---|---|---|---|---|---|---|---|
| trans. | $e_u$ | 0.0055 | 0.0309 | 0.0094 | 0.0053 | 0.0020 | 0.0053 |
| motion | $e_\theta$ | −0.0006 | 0.0003 | 0.0001 | 0.0000 | 0.0000 | 0.0000 |
| rot. | $e_u$ | 0.0065 | 0.0102 | 0.0065 | 0.0077 | 0.0077 | 0.0077 |
| motion | $e_\theta$ | −0.0009 | 0.0000 | −0.0006 | −0.0018 | 0.0002 | −0.0001 |
| helical | $e_u$ | 0.0114 | 0.0151 | 0.0130 | 0.0069 | 0.0053 | 0.0069 |
| motion | $e_\theta$ | −0.0007 | −0.0001 | −0.0007 | −0.0013 | −0.0001 | −0.0003 |

Table 5–8: Average maximum value over cycle, 2 Hz tests

| Motion | Max. | PD Exp. | CT Exp. | TS Exp. | PD Sim. | CT Sim. | TS Sim. |
|---|---|---|---|---|---|---|---|
| trans. | $\tau_{max}$ | 3.4247 | 3.2753 | 2.9411 | 2.8647 | 2.8506 | 2.8647 |
| | $e_u$ | 0.6625 | 0.6168 | 0.5425 | 0.5650 | 0.4487 | 0.5650 |
| | $e_\theta$ | 0.0123 | 0.0034 | 0.0032 | 0.0017 | 0.0017 | 0.0017 |
| rot. | $\tau_{max}$ | 2.6163 | 2.3847 | 2.3260 | 2.3623 | 2.3233 | 2.3594 |
| | $e_u$ | 0.3773 | 0.2053 | 0.2029 | 0.1972 | 0.1972 | 0.1972 |
| | $e_\theta$ | 0.0156 | 0.0077 | 0.0110 | 0.0233 | 0.0049 | 0.0118 |
| helical | $\tau_{max}$ | 2.2811 | 2.3241 | 2.4782 | 2.3586 | 2.3834 | 2.3980 |
| | $e_u$ | 0.3033 | 0.3077 | 0.3840 | 0.3718 | 0.3138 | 0.3717 |
| | $e_\theta$ | 0.0121 | 0.0076 | 0.0069 | 0.0130 | 0.0038 | 0.0072 |

Table 5–9: Experimental RMS results and percentage difference of CT, TS vs. PD controllers, 1 Hz tests

| Motion | RMS | PD Exp. | CT Exp. | TS Exp. | %Δ | CT Exp. | TS Exp. |
|---|---|---|---|---|---|---|---|
| trans. | $\bar{\tau}$ | 0.5084 | 0.4978 | 0.5052 | $\bar{\tau}$ | −2.09 | −0.63 |
| | $e_u$ | 0.1127 | 0.0479 | 0.1040 | $e_u$ | −57.50 | −7.76 |
| | $e_\theta$ | 0.0007 | 0.0006 | 0.0005 | $e_\theta$ | −14.19 | −33.10 |
| rot. | $\bar{\tau}$ | 0.2737 | 0.2750 | 0.2838 | $\bar{\tau}$ | 0.48 | 3.71 |
| | $e_u$ | 0.0031 | 0.0068 | 0.0034 | $e_u$ | 117.24 | 7.19 |
| | $e_\theta$ | 0.0067 | 0.0013 | 0.0024 | $e_\theta$ | −81.01 | −63.60 |
| helical | $\bar{\tau}$ | 0.3520 | 0.3757 | 0.3822 | $\bar{\tau}$ | 6.73 | 8.56 |
| | $e_u$ | 0.0761 | 0.0605 | 0.0740 | $e_u$ | −20.51 | −2.72 |
| | $e_\theta$ | 0.0030 | 0.0006 | 0.0011 | $e_\theta$ | −80.44 | −61.74 |

**Discussion of Results**

**Performance Assessment.** The performance of the C-drive is most readily assessed by considering the experimental data from the combined rotation and translation (helical) 2 Hz test program. The translation and rotation error curves appear in Figs. 5–1f and 5–1e. The torque curves are not shown, as they are visually indistinguishable.

The performance of all three controllers is satisfactory. Table 5–8 indicates that the maximum experimental translation and rotation errors are 0.384 mm and 0.0121 rad, respectively. The error at cycle endpoints is very low, the largest being 0.0151 mm and 0.0007 rad, according to Table 5–7.

TS and PD controllers are nearly equivalent in terms of translation error, while the CT controller has 10% higher RMS error according to Table 5–6. Large differences appear in rotation error, where TS and CT controllers achieve 63% and 81% improvements over the PD controller, respectively. Table 5–9 displays the corresponding results in the 1 Hz tests, where the improvements are nearly the same,

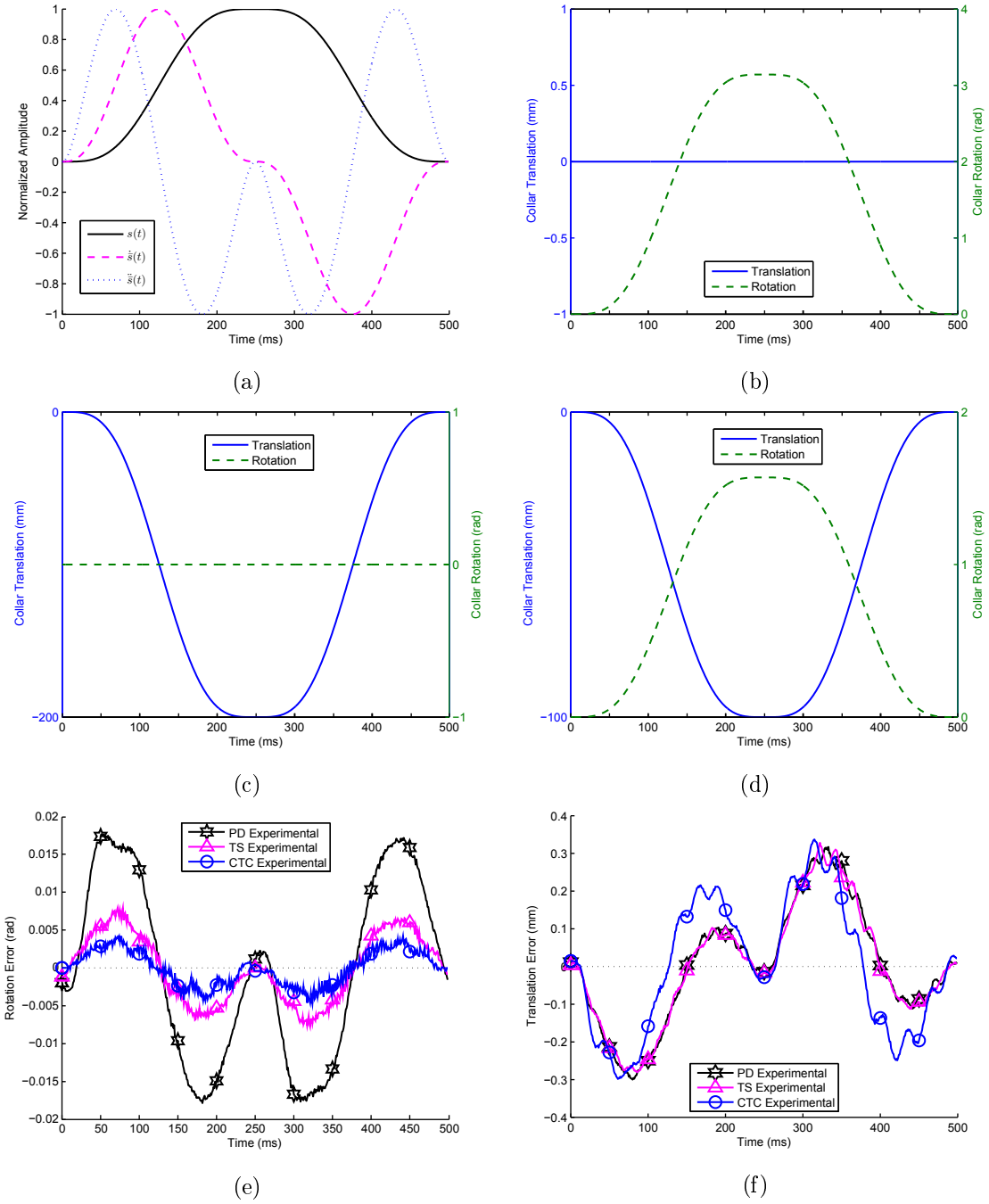


Figure 5–1: 2 Hz cycles: (a) 4-5-6-7 polynomial and normalized derivatives; (b) rotation motion program; (c) translation motion program; (d) helical motion program; and experimental helical motion tests: (e) rotation error, (f) translation error

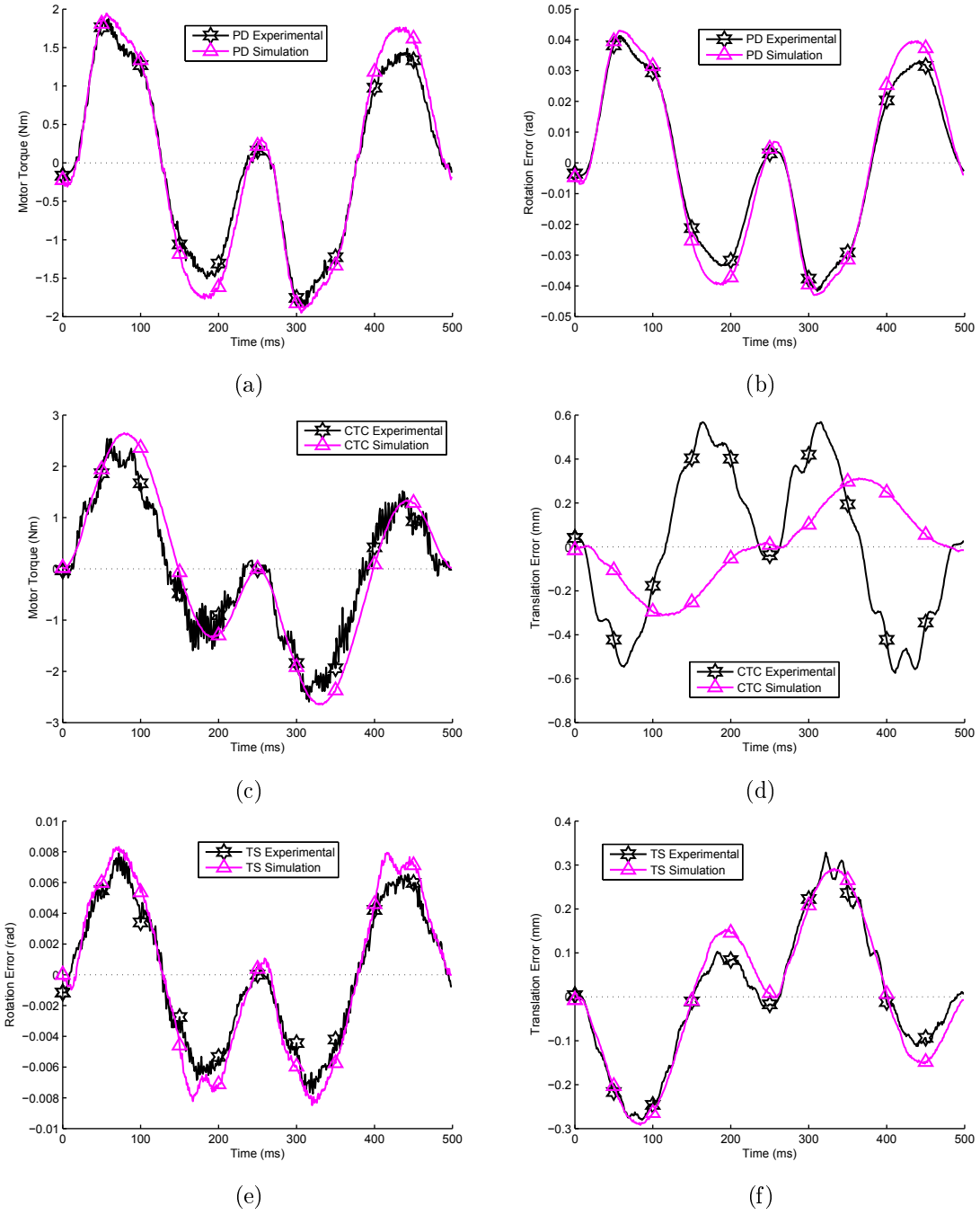


Figure 5–2: 2 Hz test results: PD controller rotation test: (a) motor torque, (b) rotation error; CTC translation test: (c) motor torque, (d) translation error; and TS controller helical test: (e) rotation error, (f) translation error

namely 62% and 80%. However, the degradation in translation error performance disappears at 1 Hz for the CT controller, this metric being improved by 20.5%. It can be surmised that the poor translation results at 2 Hz result from unmodelled dynamics that play a larger role in the presence of higher loads and speeds, or from limits in the controller bandwidth.

**Experiment vs. Simulation.** Upon visual inspection of Fig. 5–2, it is apparent that the simulated and experimental motor torques are closely matched. This is confirmed by the RMS percentage error analysis in Table 5–5: the simulations overestimate motor torques by 2.8–13.5%. Possible sources of this discrepancy are poor motor torque calibration and the underestimation of friction in the theoretical model.

The accuracy of the error simulations is fairly good for the PD and TS controllers, but poor for the CT controller. For PD and TS controllers, translation error predictions are best for the translation tests, and rotation error predictions for the rotation tests. The blank entries in Table 5–5 are due to zero error being predicted in simulations. For the CT controller, all error predictions are poor, but of the correct order of magnitude. As this is the only model-based controller, the differences between the simple linear model and the true dynamics of the C-drive are likely more pronounced in this case.

From a design perspective, one of the most important results is the predicted maximum torque, as it is used in motor dimensioning. Table 5–8 shows that the simulated results are close to experiment. The simple theoretical model is therefore good enough to dimension motor torques for future C-drive prototypes.

The predicted error at endpoints from Table 5–7 are generally of the correct order of magnitude. One likely cause of the discrepancies is the unmodelled elasticity of the ballscrews and collar.

The performance of CT and TS controllers compared to the PD controller is considered in Table 5–6. Simulations do not consistently predict the advantages and disadvantages of each type of controller in the translation motion program, while being fairly predictive for the other two motions.

## 5.2 PMC Tests

PMC operating instructions are reported in Appendix B. In the preliminary PMC tests, it was found that the motors could not produce enough torque to generate satisfactory motions. This was not predicted, as the dynamics of the PMC is not yet modelled, and the motors were reused from the old McGill SMG. In order to reduce the motor loading, a simple static balancing method was devised: the top of the PM is connect to a counterweight by a rope and pulley system above the robot. The counterweight has approximately the same mass as the PM, and enables the PMC to perform the desired motions. Low stretch braided fishing line is used as rope.

### 5.2.1 Calibration

Robot calibration is required for the controller to obtain good estimates of joint displacements and gripper pose. In this proof-of-concept testing, accurate calibration is not required. The PMC is manually placed at its isotropic posture, shown in Fig. 3–4, by inspection. The controller saves the corresponding C-drive encoder readouts and associates them with this reference posture, from which the PMC calculates all other postures using the inverse displacement analysis.

### 5.2.2 Observations

#### Motion Fidelity

The PMC successfully performs translations in all three directions throughout the workspace. Errors in positioning are too small to be visible. The performance of the PMC in rotation is much poorer. The PM rotates when subject to opposing axial forces produced by the two limbs. The transmission angles between the distal links and the PM are posture-dependent, and so are the motor torques required to rotate the PM. The central vertical region of the PMC workspace requires the largest torques, and consequently, the smallest C-drive angular displacements, to rotate the PM. In that region, the gesture is sensitive to controller, calibration and assembly error, as well as to deflections resulting from link flexibility and especially joint compliance. In summary, the PMC does not always produce de desired amplitude of rotation.

Substantial improvements in rotational performance were achieved by decreasing the compliance of the revolute joints of the proximal and distal links, thereby reducing unwanted pitching and rolling of the PM. Increasing the lubrication of the pulleys in the static balancing system also improved performance. The PMC was found to perform best in the upper part of its vertical workspace.

#### Controller Tuning

The rotational performance of the PMC is sensitive to error in C-drive rotational displacements. Higher controller gains are thus required for C-drive rotation than for translation. The TS controller is therefore used to control the PMC. The controller

gains are listed in Table 5–10. The C-drives have different proportional gains in order to prevent motor saturation, as the counterweight causes unequal loading.

Table 5–10: PMC controller settings

| C-drive # | $k_P^{trans}$ | $k_P^{rot}$ | $k_D^{trans}$ | $k_D^{rot}$ | N |
|---|---|---|---|---|---|
| I | 35 | 105 | 0.1 | 0.09 | 600 |
| II | 35 | 52.5 | 0.1 | 0.09 | 600 |
| Units | Nm/rad | Nm/rad | Nms/rad | Nms/rad | rad/s |

### 5.2.3 Industry Standard Test Trajectory

The unsmoothed test trajectory described in Section 2.1.2 is produced by the PMC, as an optimal path is not required for this proof of concept. The path between segment points is interpolated by 4-5-6-7 polynomials, described in Section 5.1.4. The duration of segments AB and CD was 350 ms each, while segment BC lasted 1000 ms. The cycle frequency is therefore 0.3 Hz. Faster cycle times were possible, but led to significant vibrations of the PM . A video of the PMC performing this test motion is posted at the following links:

http://www.cim.mcgill.ca/∼rmsl/Index/research.htm

https://youtu.be/m9ieYH4QkYE

**Results**

The PMC prototype successfully produces the test motion, thereby proving that the robot concept is viable. The motion appears visually correct. Upon close inspection, a slight pitch and roll of the PM can be seen. In addition, the rotational amplitude of the PM is not exactly $\pi$ rad, and is faster in one direction than the other. The three translational motions appear satisfactory.

# CHAPTER 6
# Conclusions and Recommendations

PMC forward and inverse displacement analyses were formulated for all assembly modes of the robot, and validated experimentally for the elbow-up forearm-down kinematics branch in which the prototype operates. The visualisation and verification of these results were aided by the introduction of planar PMC diagrams. Employing the foregoing analyses, the reachable workspace of the PMC was derived, allowing for the safe operation of the robot.

Premiere C-drive and PMC prototypes were designed, built, tested, and shown to operate as intended. The PMC prototype successfully produced the standard industry test trajectory at 0.3 Hz, though with inconsistent performance in rotating the gripper. The C-drives demonstrated good performance in benchmark tests with three different control schemes. The simple linear dynamic model of the C-drive, which was employed for simulation, state estimation and model-based control, yielded satisfactory results. The model-based controller produced the best results overall, including up to 81% reduction in rotation error as compared to a simple PD controller.

Although the C-drive dynamics model was shown to be sufficiently accurate for motor dimensioning, it is recommended that a nonlinear C-drive model now be developed, for improved performance in simulation and control. Specifically, Coulomb friction and the internal dynamics of the motors—which had been assumed to perform

ideally—should be included. Furthermore, a task-space approach is recommended for the control of the PMC, by virtue of the simplicity of the robot kinematics. The model-based resolved-acceleration controller [48] is suggested, once the PMC dynamics is derived.

Improvements to the mechanical design of the PMC would enhance performance, particularly in rotating the gripper. A shorter PepperMill—and smaller vertical distance between the C-drives—would increase the rigidity of the PMC, and hence its rotational performance. Moreover, the proximal and distal link lengths need not be identical, and stand to be optimized for maximum PM rotation torque. To this end, the analogy between a single limb and a slider-crank mechanism is proposed: the threaded Hooke joint, which translates in the direction of the axis of the PM, corresponds to the slider. Well-known methods of solution can then be employed. Finally, the prototype revolute joints should be redesigned for higher stiffness.

The PMC is statically balanced by means of a counterweight system, which reduces torque requirements at low speeds at the cost of adding to the driven mass. Loading on the drives could be reduced substantially at high speeds by redesigning the links to achieve dynamic balancing. Further research on this problem is recommended with the aim of increasing the speed of the PMC.

# Appendix A

| Category | Pn No. | Code | Description | Value | Units | Servo | Min | Max | Default |
|---|---|---|---|---|---|---|---|---|---|
| Basic Switch | Pn000 | BPRM0 | Function Selection Basic Switch 1 | 0020 | -- | 0020 | | | 0000 |
| App Switch | Pn001 | BPRM1 | Function Selection Application Switch 1 | 0000 | -- | 0000 | | | 0000 |
| App Switch | Pn002 | BPRM2 | Function Selection Application Switch 2 | 0000 | -- | 0000 | | | 0000 |
| App Switch | Pn003 | BPRM3 | Function Selection Application Switch 3 | 0002 | -- | 0002 | | | 0002 |
| Gain | Pn100 | LOOPHZ | Speed Loop Gain | 40 | Hz | 40 | 1 | 2000 | 40 |
| Gain | Pn101 | PITIME | Speed Loop Integration Time Constant | 2000 | 0.01ms | 2000 | 15 | 51200 | 2000 |
| Gain | Pn102 | POSGN | Position Loop Gain | 40 | 1/s | 40 | 1 | 2000 | 40 |
| Gain | Pn103 | JLOAD | Inertia Ratio | 0 | % | 0 | 0 | 10000 | 0 |
| Gain | Pn104 | LOOPHZ2 | 2nd Speed Loop Gain | 40 | Hz | 40 | 1 | 2000 | 40 |
| Gain | Pn105 | PITIME2 | 2nd Speed Loop Integration Time Const | 2000 | 0.01ms | 2000 | 15 | 51200 | 2000 |
| Gain | Pn106 | POSGN2 | 2nd Position Loop Gain | 40 | 1/s | 40 | 1 | 2000 | 40 |
| Gain | Pn107 | BIASLV | Bias Level | 0 | rpm | 0 | 0 | 450 | 0 |
| Gain | Pn108 | BIASAD | Bias Width Addition | 7 | ref units | 7 | 0 | 250 | 7 |
| Gain | Pn109 | FFGN | Feed Forward | 0 | % | 0 | 0 | 100 | 0 |
| Gain | Pn10A | FFFILT | Feed Forward Filter Time Constant | 0 | 0.01ms | 0 | 0 | 6400 | 0 |
| Gain | Pn10B | GNMODE | Gain-Related Application SW | 0000 | -- | 0000 | | | 0000 |
| Gain | Pn10C | TRQMSW | Mode Switch (Torque Reference) | 200 | % | 200 | 0 | 800 | 200 |
| Gain | Pn10D | REFMSW | Mode Switch (Speed Reference) | 0 | rpm | 0 | 0 | 10000 | 0 |
| Gain | Pn10E | ACCMSW | Mode Switch (Acceleration Reference) | 0 | 10rpm/s | 0 | 0 | 3000 | 0 |
| Gain | Pn10F | ERPMSW | Mode Switch (Error Pulse) | 0 | ref units | 0 | 0 | 10000 | 0 |
| Gain | Pn110 | RTAT | Online Auto Tuning Related SW | 0010 | -- | 0010 | | | 0010 |
| Gain | Pn111 | VOBGN | Speed Feedback Compensation | 100 | % | 100 | 1 | 500 | 100 |
| Position | Pn200 | PRSTSW | Position Control Configuration Command | 0000 | -- | 0000 | | | 0000 |
| Position | Pn201 | PGRAT | PG Division Ratio | 8192 | P/R | 8192 | 16 | 16384 | 16384 |
| Position | Pn202 | RATB | Electronic Gear Ratio (Numerator) | 1 | -- | 1 | 1 | 65535 | 4 |
| Positon | Pn203 | RATA | Electronic Gear Ratio (Denominator) | 1 | -- | 1 | 1 | 65535 | 1 |
| Position | Pn204 | ACCTIM | Position Reference Acc/Dec Constant | 0 | 0.01ms | 0 | 0 | 6400 | 0 |
| Position | Pn205 | MTLMT | Multi Turn Limit | 65535 | rev | 65535 | 0 | 65535 | 65535 |
| Position | Pn207 | CMFILSW | Position Reference Function SW | 0000 | -- | 0000 | | | 0000 |
| Position | Pn208 | S_CMFIL | Position Reference S Filter Time Constar | 0 | 0.01ms | 0 | 0 | 6400 | 0 |
| Speed | Pn300 | VREFGN | Speed Reference Gain | 600 | 0.01V/rated spe | 600 | 150 | 3000 | 600 |
| Speed | Pn301 | SPEED1 | Internal Set Speed (1st speed) | 100 | rpm | 100 | 0 | 10000 | 100 |
| Speed | Pn302 | SPEED2 | Internal Set Speed (2nd speed) | 200 | rpm | 200 | 0 | 10000 | 200 |
| Speed | Pn303 | SPEED3 | Internal Set Speed (3rd speed) | 300 | rpm | 300 | 0 | 10000 | 300 |
| Speed | Pn304 | JOGSPD | Jog Speed | 500 | rpm | 500 | 0 | 10000 | 500 |
| Speed | Pn305 | SFSACC | Soft Start Time (Acceleration) | 0 | ms | 0 | 0 | 10000 | 0 |
| Speed | Pn306 | SFSDEC | Soft Start Time (Deceleration) | 0 | ms | 0 | 0 | 10000 | 0 |
| Speed | Pn307 | SRFIL | Speed Reference Filter Time Constant | 40 | 0.01ms | 40 | 0 | 65535 | 40 |
| Speed | Pn308 | FBFIL | Speed FB Filter Time Constant | 0 | 0.01ms | 0 | 0 | 65535 | 0 |
| Torque | Pn400 | TCRFGN | Torque Reference Gain | 35 | 0.1V/rated torqu | 35 | 10 | 100 | 30 |
| Torque | Pn401 | TRQFIL | Torque Reference Filter Time Constant | 60 | 0.01ms | 60 | 0 | 65535 | 100 |
| Torque | Pn402 | TLMTF | Forward Rotation Torque Limit | 100 | % | 100 | 0 | 800 | 800 |
| Torque | Pn403 | TLMTR | Reverse Rotation Torque Limit | 100 | % | 100 | 0 | 800 | 800 |
| Torque | Pn404 | CLMIF | Forward External Torque Limit | 100 | % | 100 | 0 | 800 | 100 |
| Torque | Pn405 | CLMIR | Reverse External Torque Limit | 100 | % | 100 | 0 | 800 | 100 |
| Torque | Pn406 | EMGTRQ | Emergency Stop Torque | 800 | % | 800 | 0 | 800 | 800 |
| Torque | Pn407 | TCRLMT | Torque Control Speed Limit | 5000 | rpm | 5000 | 0 | 10000 | 10000 |
| Torque | Pn408 | TFUNCSW | Torque Control Function SW | 0000 | -- | 0000 | | | 0000 |

Servo Amplifier Settings (Torque Control Mode is used)

# Appendix B

## PepperMill-Carrier Operation Protocol

Training is mandatory before operating PMC robot

### STARTING THE ROBOT

**Step 1:** Visually inspect robot to ensure that all safety panels are secured and that the enclosure is free of obstructions.

**Step 2:** Turn on Brighella computer. The Target computer should always be kept on to maintain robot calibration.

**Step 3:** Open RT-Lab Metacontroller from Start Menu. Load PMCcontroller.mdl

**Step 4:** Ensure that Motor Torque Saturation is set to 0, then click Execute.

**Step 5:** Turn power switch of control box to ON (1) and press Reset button. Plug in both Red and Green sensor power supplies.

### OPERATING THE ROBOT

**Info:** The standard industry test-cycle at 0.5 Hz is preloaded into the program. Its x, y, z and phi motion amplitudes are multiplied by scalar gains. The speed of the overall cycle can be slowed down.

**Step 1:** Select the motion gains. [1 1 1 2] produces the standard cycle.

**Step 2:** Select the time constant as an integer between 1 and 10. The value 1 corresponds to 0.5 Hz operation, while 10 is 0.05 Hz.

**Step 3:** Select the overall Motion Amplitude between 0 and 1. This parameter multiplies the motion gains. The value 1 is standard.

**Step 4:** The motors only run while hand-held safety switch is depressed. Keep it depressed through the next steps. Releasing it cuts power to the motors.

**Step 5:** Set Motor Torque Saturation to 1, then 10 when home position reached.

**Step 6:** Engage Start Robot software switch. The robot performs one test-cycle.

**Step 7:** Engage Repeat software switch for the robot to repeat cycle indefinitely.

### SHUTTING DOWN THE ROBOT

**Step 1:** Disengage Repeat, wait for cycle to end, disengage Start Robot, release hand-held switch, set Motor Torque Saturation to 0.

**Step 2:** Click Reset in the Metacontroller to close program.

**Step 3:** Switch off power button on control box, unplug both power supplies.

Robot Specifications: Maximum Instantaneous Values at End Effector

| | Horizontal | Vertical |
|---|---|---|
| Force | 640 N | 32 N |
| Velocity | 660 mm/s | 110 mm/s |

**Robot cannot carry payload**

*Thomas Friedlaender, April 2015*

References

[1] Westerlund, L., *The Extended Arm of Man: A History of the Industrial Robot.* Informationsförlaget, 2000.

[2] Angeles, J., *Design Challenges in the Development of Fast Pick-and-place Robots.* Springer, 2013.

[3] Hervé, J., "The lie group of rigid body displacements, a fundamental tool for mechanism design," *Mechanism and Machine theory*, vol. 34, no. 5, pp. 719–730, 1999.

[4] Makino, H., Kato, A., and Yamazaki, Y., "Research and commercialization of scara robot–the case of industry-university joint research and developmentâăť," *International Journal of Automation Technology*, vol. 1, pp. 61–67, 2007.

[5] Pandilov, Z. and Dukovski, V., "Comparison of the characteristics between serial and parallel robots," *Acta Technica Corviniensis-Bulletin of Engineering*, vol. 7, no. 1, p. 143, 2014.

[6] Gough, V. and Whitehall, S., "Universal tyre test machine," in *Proc. FISITA 9th Int. Technical Congress*, 1962, pp. 117–137.

[7] Bonev, I., "The true origins of parallel robots," *ParalleMIC: The Parallel Mechanisms Information Center*, 2003.

[8] Clavel, R., *Device for the movement and positioning of an element in space*, US Patent 4,976,582, 1990.

[9] Hervé, J. M. and Sparacino, F., "Star, a new concept in robotics," in *Fifth International Conference on Advanced Robotics*, Citeseer, 1991.

[10] Pierrot, F., Shibukawa, T., Morita, K., *et al.*, *Four-degree-of-freedom parallel robot*, US Patent 6,516,681, 2003.

[11] Krut, S., Benoit, M., Ota, H., and Pierrot, F., "I4: A new parallel mechanism for scara motions," in *Robotics and Automation, 2003. Proceedings. ICRA'03. IEEE International Conference on*, IEEE, vol. 2, 2003, pp. 1875–1880.

[12] Richard, P.-L., Gosselin, C. M., and Kong, X., "Kinematic analysis and prototyping of a partially decoupled 4-dof 3t1r parallel manipulator," *Journal of Mechanical Design*, vol. 129, no. 6, pp. 611–616, 2007.

[13] Angeles, J., Caro, S., Khan, W., and Morozov, A., "Kinetostatic design of an innovative schönflies-motion generator," *Proceedings of the Institution of Mechanical Engineers, Part C: Journal of Mechanical Engineering Science*, vol. 220, no. 7, pp. 935–943, 2006.

[14] Cammarata, A., Angeles, J., and Sinatra, R., "Kinetostatic and inertial conditioning of the Mcgill Schönflies-motion generator," *Advances in Mechanical Engineering*, vol. 2, p. 186 203, 2010.

[15] Lee, C.-C. and Hervé, J. M., "Generators of the product of two Schoenflies motion groups," *European Journal of Mechanics-A/Solids*, vol. 29, no. 1, pp. 97–108, 2010.

[16] Lee, C.-C. and Hervé, J. M., "Isoconstrained parallel generators of Schoenflies motion," *Journal of Mechanisms and Robotics*, vol. 3, no. 2, p. 021 006, 2011.

[17] Lee, P.-C. and Lee, J.-J., "Singularity and workspace analysis of three isoconstrained parallel manipulators with schoenflies motion," *Frontiers of Mechanical Engineering*, vol. 7, no. 2, pp. 163–187, 2012.

[18] Lee, P.-C. and Lee, J.-J., "On the kinematics of a new parallel mechanism with Schoenflies motion," *Robotica*, pp. 1–15,

[19] Lee, P.-C., Lee, J.-J., and Lee, C.-C., "Four novel pick-and-place isoconstrained manipulators and their inverse kinematics," in *ASME 2010 International Design Engineering Technical Conferences and Computers and Information in Engineering Conference*, American Society of Mechanical Engineers, 2010, pp. 1079–1088.

[20] Lee, P.-C. and Lee, J.-J., "Forward kinematics and numerical verification of four novel parallel manipulators with schoenflies motion," in *Proceedings of the 1st IFToMM Asian Conference on Mechanical Machine Science, Taipei*, 2010.

[21] Harada, T. and Angeles, J., "Kinematics and singularity analysis of a CR-RHHRRC parallel schönflies motion generator," *Transactions of the Canadian Society for Mechanical Engineering*, vol. 38, no. 2, pp. 173–183, 2014.

[22] Angeles, J., "The degree of freedom of parallel robots: A group-theoretic approach," in *Robotics and Automation, 2005. ICRA 2005. Proceedings of the 2005 IEEE International Conference on*, IEEE, 2005, pp. 1005–1012.

[23] Behi, F., "Kinematic analysis for a six-degree-of-freedom 3-prps parallel mechanism," *Robotics and Automation, IEEE Journal of*, vol. 4, no. 5, pp. 561–565, 1988.

[24] Kohli, D., Lee, S.-H., Tsai, K.-Y., and Sandor, G., "Manipulator configurations based on rotary-linear (rl) actuators and their direct and inverse kinematics," *Journal of Mechanical Design*, vol. 110, no. 4, pp. 397–404, 1988.

[25] Kohli, D. and Sandor, G. N., *Rotary linear actuator for use in robotic manipulators*, US Patent 4,806,068, 1989.

[26] Harada, T., Friedlaender, T., and Angeles, J., "The development of an innovative two-dof cylindrical drive: Design, analysis and preliminary tests," in *Robotics and Automation (ICRA), 2014 IEEE International Conference on*, IEEE, 2014, pp. 6338–6344.

[27] Khan, W. A. and Angeles, J., "A novel paradigm for the qualitative synthesis of simple kinematic chains based on complexity measures," *Journal of Mechanisms and Robotics*, vol. 3, no. 3, p. 031 010, 2011.

[28] Trézières, D., Harada, T., and Angeles, J., *Mechanical design of a new Schönflies-Motion Generator, TR-CIM-13-01.*

[29] Friedlaender, T. and Angeles, J., "Dynamics and control of a novel two-degree-of-freedom drive," in *2015 ECCOMAS Thematic Conference on Multibody Dynamics, Extended Abstract, Barcelona, Spain, June 29– July 2*, 2015.

[30] Strang, G., *Introduction to Linear Algebra.* Wellesley-Cambridge Press, 2003, ISBN: 9780961408893.

[31] Choi, H.-B., Company, O., Pierrot, E, Konno, A., Shibukawa, T, and Uchiyama, M., "Design and control of a novel 4-dofs parallel robot H4," in *Robotics and Automation, 2003. Proceedings. ICRA'03. IEEE International Conference on*, IEEE, vol. 1, 2003, pp. 1185–1190.

[32] Gauthier, J.-F., Angeles, J, and Nokleby, S, "Optimization of a test trajectory for scara systems," in *Advances in Robot Kinematics: Analysis and Design*, Springer, 2008, pp. 225–234.

[33] Forsythe, G. E., "Pitfalls in computation, or why a math book isn't enough," English, *The American Mathematical Monthly*, vol. 77, no. 9, pp. 931–956, 1970, ISSN: 00029890. [Online]. Available: `http://www.jstor.org/stable/2318109`.

[34] Merlet, J.-P., *Parallel Robots*. Springer Science & Business Media, 2012, vol. 74.

[35] Angeles, J., Caro, S., Hirigoyen, G., Khan, W., Morozov, A., Salerno, A., and Smith, J., *The Design, Prototyping, Interfacing, and Control of an Innovative Schönflies-Motion Generator, TR-CIM 06.05*.

[36] Watkins, D. S., *Fundamentals of Matrix Computations*. John Wiley & Sons, 2004, vol. 64.

[37] Kailath, T., *Linear systems*. Prentice-Hall Englewood Cliffs, NJ, 1980.

[38] Bryson Jr, A. E. and Luenberger, D. G., "The synthesis of regulator logic using state-variable concepts," *Proceedings of the IEEE*, vol. 58, no. 11, pp. 1803–1811, 1970.

[39] Ogata, K., *Matlab for Control Engineers*. Pearson Prentice Hall, 2008.

[40] MATLAB, *Version 7.12.0 (R2011a)*. Natick, Massachusetts: The MathWorks Inc., 2011.

[41] Visioli, A., *Practical PID control*. Springer Science & Business Media, 2006.

[42] Ellis, G., *Control System Design Guide: Using your Computer to understand and diagnose Feedback Controllers*. Butterworth-Heinemann, 2012.

[43] An, C. H., Atkeson, C. G., and Hollerbach, J. M., *Model-based Control of a Robot Manipulator*. MIT press Cambridge, MA, 1988, vol. 214.

[44] Markiewicz, B., "Analysis of the computed torque drive method and comparison with conventional position servo for a computer-controlled manipulator," 1973.

[45] Khosla, P. K. and Kanade, T., "Real-time implementation and evaluation of the computed-torque scheme," *Robotics and Automation, IEEE Transactions on*, vol. 5, no. 2, pp. 245–253, 1989.

[46] Srinivas, J., Dukkipati, R., and Ramji, K., *Robotics: Control and Programming*. Alpha Science International, 2009, ISBN: 9781842654934.

[47] Ramesh, R., Mannan, M., and Poo, A., "Tracking and contour error control in cnc servo systems," *International Journal of Machine Tools and Manufacture*, vol. 45, no. 3, pp. 301–326, 2005.

[48] Caccavale, F., Natale, C., Siciliano, B., and Villani, L., "Resolved-acceleration control of robot manipulators: A critical review with experiments," *Robotica*, vol. 16, no. 05, pp. 565–573, 1998.

[49] Åström, K. J. and Wittenmark, B., *Computer-controlled Systems: Theory and Design*. Courier Corporation, 2011.

[50] Virgala, I. and Kelemen, M., "Experimental friction identification of a dc motor," *International Journal of Mechanics and Applications*, vol. 3, no. 1, pp. 26–30, 2013.